PB86-122595

Development of Advanced ESFF (Electrical Stimulation of Fabric Filtration) Technology

Textile Research Inst., Princeton, NJ

Prepared for

Environmental Protection Agency
Research Triangle Park, NC

Oct 85

U.S. Department of Commerce
National Technical Information Service
NTIS.

PB86-122595

EPA/600/7-85/049
October 1985

DEVELOPMENT OF ADVANCED ESFF TECHNOLOGY

by

George E. R. Lamb, Richard I. Jones, Kathleen T. Duffy,
Dudley A. Saville, and Barry A. Morris

Textile Research Institute
P. O. Box 625
Princeton, New Jersey 08542

Environmental Protection Agency
Cooperative Agreement CR 808875

EPA Project Officer:

Louis S. Hovis
Air and Energy Engineering Research Laboratory
Research Triangle Park, North Carolina 27711

AIR AND ENERGY ENGINEERING RESEARCH LABORATORY
OFFICE OF RESEARCH AND DEVELOPMENT
U.S. ENVIRONMENTAL PROTECTION AGENCY
RESEARCH TRIANGLE PARK, NC 27711

REPRODUCED BY
NATIONAL TECHNICAL
INFORMATION SERVICE
U.S. DEPARTMENT OF COMMERCE
SPRINGFIELD, VA. 22161

TECHNICAL REPORT DATA (Please read Instructions on the reverse before completing)		
1. REPORT NO. EPA/600/7-85/049	2.	3. RECIPIENT'S ACCESSION NO. PB86 122595/AS
4. TITLE AND SUBTITLE Development of Advanced ESFF Technology		5. REPORT DATE October 1985
		6. PERFORMING ORGANIZATION CODE
7. AUTHOR(S) G. E. R. Lamb, R. I. Jones, K. T. Duffy, D. A. Saville, and B. A. Morris		8. PERFORMING ORGANIZATION REPORT NO.
9. PERFORMING ORGANIZATION NAME AND ADDRESS Textile Research Institute P. O. Box 625 Princeton, New Jersey 08540		10. PROGRAM ELEMENT NO.
		11. CONTRACT/GRANT NO. CR 808875
12. SPONSORING AGENCY NAME AND ADDRESS EPA, Office of Research and Development Air and Energy Engineering Research Laboratory Research Triangle Park, NC 27711		13. TYPE OF REPORT AND PERIOD COVERED Final; 5/82 - 5/85
		14. SPONSORING AGENCY CODE EPA/600/13
15. SUPPLEMENTARY NOTES AEERL project officer is Louis S. Hovis, Mail Drop 61, 919/541-3374.		

16. ABSTRACT The report summarizes work on electrical stimulation of fabric filtration (ESFF) with the major objectives of defining the role of some primary variables and understanding the mechanisms of electrostatic enhancement. It was concluded that the magnitude of particle charge has a strong effect on ESFF performance by causing shifts in dust deposition from a uniform pattern to a selective deposition along the electrodes in the bag and toward the bottom half of the bag. The drastic reduction in pressure drop indicated that some form of precharging would be cost effective. Programmed changes in electrical field strength to coincide with the cleaning cycle or the use of ac rather than dc fields showed no significant promise of improved bag cleaning. "Printed" electrodes could be as effective as wire electrodes and would probably cost less to incorporate in the bag if they could be made to hold up under bag flexing at elevated temperatures.

17. KEY WORDS AND DOCUMENT ANALYSIS		
a. DESCRIPTORS	b. IDENTIFIERS/OPEN ENDED TERMS	c. COSATI Field/Group
Pollution	Pollution Control	13B
Particles	Stationary Sources	14G
Dust	Particulate	11G
Filtration	Baghouses	07D
Fabrics	Fabric Filters	11E
Electrostatics	Precharging	20C
18. DISTRIBUTION STATEMENT Release to Public	19. SECURITY CLASS (This Report) Unclassified	21. NO. OF PAGES 94
	20. SECURITY CLASS (This page) Unclassified	22. PRICE

EPA Form 2220-1 (9-73)

NOTICE

This document has been reviewed in accordance with U.S. Environmental Protection Agency policy and approved for publication. Mention of trade names or commercial products does not constitute endorsement or recommendation for use.

ABSTRACT

This report describes work done to explore means for magnifying the effects and broadening the scope of electrical stimulation of fabric filtration (ESFF). The importance of these effects was established in earlier work, both in the laboratory and in pilot plant trials. The present work covered a number of separate topics: 1) the effects of particle charge levels, 2) studies of the mechanisms of pressure drop reduction, 3) programming of the applied electric fields with respect to time, 4) a study of the cleaning of fabric filters, and 5) the use of printed electrodes.

The results show that particle charge has a strong effect on the response of filtration performance to ESFF and that some form of precharging device would be cost-effective in many cases. Measurements of dust deposition patterns show that electrical effects cause shifts in the dust deposits a) towards the entrance of the bag, b) to the electrodes, and c) towards the surface of the fabric. Results of modeling studies agree quantitatively with the observed effects. Studies of programmed voltages examined the possibility of using sudden changes in electric field to aid bag cleaning and also the effects of using AC rather than DC fields, but neither approach holds out promise of significantly improved performance. When pulse-cleaned bags were run at higher than conventional velocities, penetration rose to unacceptable levels, whereas with bags cleaned with reverse air, pressure drop reached large values; the difference appears to be related to the energy levels of the two cleaning methods. "Printed" electrodes are stripes of conducting material replacing metal wire electrodes and having the advantages of lower cost and the possibility of applying electrodes of complicated design; they appear to be as effective as wire electrodes.

This report was submitted in fulfillment of Cooperative Agreement CR 808875 by the Textile Research Institute under the sponsorship of the U. S. Environmental Protection Agency. This report covers the period from May 1, 1981, to October 30, 1984, and work was completed in October 1984.

CONTENTS

Abstract	ii
List of Figures	v
List of Tables	ix
1. Introduction	1
2. Conclusions	2
3. Recommendations	4
4. Effects of Particle Charge Levels	5
Lightning Rod Precharger	5
Mechanisms of Pressure Drop Reduction	10
Permeability Scanning	19
Electric Field and Particle Trajectories in an ESFF Bag	21
Particle Size Distribution as a Function of Location in an ESFF Bag	29
5. Printed Electrodes	31
6. Programmed Voltages	34
7. Cleaning of Fabric Filters	40
Background	40
Experimental Procedures	41
Pulse-Jet Runs	41
Reverse Air Runs with Shaking	44
Cleaning by Bag Shearing	46
8. Pressure Drop Reduction by Upstream Displacement of Dust Cake	48
Introduction	48
Experiments with Two-Layer Filters	48
Results and Discussion	50
Cross-Sectional Views	50
Pressure Drop Distribution	55
Appendix 8A	59

9. Modeling of Pressure Drop Across Dust Laden Filters 60
Introduction 60
Clean Filter 60
Dust Loading 61
Case 1: Uniform Deposition 63
Case 2: Dendrite Model 64
Case 3: Combined Model 65
Fiber Volume Fraction Distribution 66
Results and Discussion 66
Implications of the Combined Model 66
Comparison with Experimental Data 71
Appendix 9A: Drag on an Isolated Porous Cylindrical Annulus in Creeping Flow 75

References 80

FIGURES

Number		Page
1	Location of "lightning rod" precharger in reverse air baghouse.	6
2	Dependence of PDR on bag field after extended run for a woven glass reverse air bag.	6
3	ESFF fading with a woven glass pulse-jet bag, and recovery of low PDR by using the precharger.	7
4	Dust deposition pattern with 4 kV/cm field and -15 kV precharger potential.	10
5	Distribution of dust mass with respect to distance from the bottom of the bag.	11
6	Appearance of the inner surface of the bag: a) after vacuum cleaning through a wire screen. b) with an average of 7.5 mg/cm^2 of fly ash deposited with no electric field or precharging.	13
7	Appearance of the inner surface of the bag: a) after deposition with 4 kV/cm between bag electrodes and +15 kV on the precharger. b) after deposition with 4 kV/cm between bag electrodes and -15 kV on the precharger.	14
8	Appearance of the inner surface of the bag: a) after deposition with 4 kV/cm between bag electrodes and no precharging. b) with positive precharging only. c) with negative precharging only.	15
9	Dependence of efficiency on face velocity for woven glass bag with and without ESFF.	17
10	Permeability of dust cake deposited with (+4,-15) at various filter bag locations and for the bag as a whole.	20

FIGURES
(continued)

Number		Page
11	Dust cake mass deposited with (+4,-15) at various locations on the inner surface of the filter bag.	20
12	Faraday cage for the measurement of particle charge due to precharging.	22
13	Charge/mass ratio as a function of precharger voltage for a fly ash aerosol stream.	22
14	Particle charge as a function of particle size.	23
15	Charge distribution assumed for calculations leading to trajectories in Figures 16, 17, and 18.	25
16	Trajectories of particles 1 μm in diameter.	27
17	Trajectories of particles 3 μm in diameter.	27
18	Trajectories of particles 10 μm in diameter.	27
19	Field intensity on radial planes passing through the electrodies.	28
20	Radial velocities for particles of indicated diameters moving in radial planes through electrodes.	28
21	Cumulative distributions with respect to particle size for dust deposited at the top and bottom of a bag run at (+4,-15).	30
22	PDR-field relationship for new (unconditioned) polyester felt patch filter having printed electrodes.	31
23	Performance of polyester felt bag fitted with printed electrodes and napped.	31
24	Effect of reverse polarity voltage during cleaning on initial pressure drop in following cycle.	35
25	Initial and final pressure drops while conditioning a woven glass filter.	36
26	Dependence of "filtering" cake resistance on mass of "conditioning" dust.	36
27	The effect of applied field on pressure drop.	38
28	Dependence of average pressure drop on face velocity and running time for a Teflon® bag cleaned by pulse-jet.	42

FIGURES
(continued)

Number		Page
29	Dependence of average pressure drop on face velocity and running time for a woven glass bag cleaned by pulse-jet.	42
30	Dependence of penetration on face velocity and time for the conditions corresponding to Figure 28.	43
31	Dependence of penetration on face velocity and time for the conditions corresponding to Figure 29.	43
32	Dependence of penetration on face velocity and running time. Teflon® bag cleaned by reverse air.	45
33	As Figure 32, but with 4 kV/cm average field on bag, -15 kV on precharger (+4,-15).	45
34	Dependence of average pressure drop on face velocity and running time with (+4,-15).	45
35	Schematic of filter apparatus.	49
36	Effect of applied potential on dust distribution in a 3-layer filter.	51
37	Effect of dust loading on its distribution in a 3-layer filter with no applied potential.	51
38	Dust distribution and corresponding pressure drop in a 2-layer filter as a function of applied potential for one dust loading (11.9 mg/cm^2) and velocity (3 cm/s).	51
39	Top views of dust cakes formed with and without an applied electric field.	52
40	Schematic of fixation process.	53
41	Cross sections of two-layer filters, the upper layer of low solidity, the lower layer of high solidity. Dust particles deposited with and without an applied electric field.	54
42	Pressure drop vs. time for a low solidity filter layer at low potentials ($\leq$1 kV).	57
43	Pressure drop vs. dust loading and filter solidity for 0 kV.	57

FIGURES
(continued)

Number		Page
44	Pressure drop across upstream layer of a 2-layer filter at several applied potentials.	57
45	Pressure drop across downstream layer of a 2-layer filter at several applied potentials.	57
46	Comparison of results of pressure drop measurements on a column packed with PET fibers with the Happel cell model for fibers parallel to the flow.	61
47	Dust cake representations. a) Uniform deposition model b) Dendrite model c) Combined model	64
48	Model results: pressure drop vs. dust loading.	68
49	Model results: pressure drop vs. ε_c.	68
50	Model results: pressure drop vs. dendrite fraction.	68
51	Model results: pressure drop as a function of dust loading for several dendrite fractions.	68
52	The effect of dust loading on a^2R^{-2} and $f(\varepsilon)$ and the resulting pressure drop.	70
53	Schematic of model representation of experimental two-layer filters.	71
54	Comparison of model results with single-layer experimental results at 0 kV applied potential.	73
55	Comparison of model predictions with two-layer experiments at a constant dust loading.	73
9A1	The porous cylinder problem.	75
9A2	Drag on a porous cylinder for a Reynolds number ($2\rho UR_2/\mu$) of 0.2 as a function of permeability k and radius ratio $R = R_1/R_2$.	78

TABLES

Number		Page
1	Pressure Drop Ratios with ESFF and Precharged Aerosol	9
2	Mass of Dust Collected on Bag in 15 Minutes	16
3	Distribution of Dust Areal Densities (mg/cm^2) on Reverse Air Bag on Positive, Ground, and Between Electrode Wires	18
4	Pressure Drops for Polyester Felt Bag with Printed Electrodes	32
5	Comparison of PDR Values with Printed and Wire Electrodes	33
6	Performance with DC and AC Voltages on Bag and DC Voltage on Precharger.	38
7	Performance with DC and AC Voltages on Bag and Precharger	39
8	Current Passed by Bags with Applied AC and DC Voltages	39
9	Ratio of Pressure Drop After Twisting to that Without Twisting at Several Twist Angles and Numbers of Twists	47
10	Comparison of Pressure Drops After Shear and Shaker Cleaning	47
11	Components of Spurr's Low Viscosity Embedding Medium	55
8A1	Particle Size Distribution for a Sample of Mercer County, New Jersey, Fly Ash (Impactor Analysis)	59
12	Physical Properties of Model Filter	72
9A1	Permeability Parameter Φ for Several Porosities, ε, as Computed From Rudnick and First's Model [21]	79

SECTION 1

INTRODUCTION

The purpose of the work described in this report was to promote the effective use of a promising technique, described in an earlier report [1] and in various other publications [2, 3], whereby the performance of fabric filters is improved by electrical effects obtained by the application of fairly large potentials to wires positioned near or on the fabric.

This electrical stimulation of fabric filters, or ESFF, can reduce both pressure drop and penetration, and this could be used to achieve better levels of pollution control, or to lower costs of operations, or both. Its most valuable feature would be the possibility of operating baghouses at higher face velocities, which has been shown to be the route to greatest savings. For this reason, parts of the present report are addressed to problems associated with higher than conventional face velocities, mainly fabric cleaning.

ESFF has already been tested in two pilot plant studies, each of which has demonstrated the feasibility of the principle under field conditions. Progress toward full-scale utilization of the technique depends on continued testing and also on the gathering of relevant basic information, which is the objective of the work reported here.

SECTION 2

CONCLUSIONS

The electric stimulation of fabric filters is strongly dependent on the level of charge on the incoming particles. If the electrode wires can be kept clear of dust cake, charging of the dust by corona from the electrodes is sufficient to reduce pressure drop by an order of magnitude. Failing that, the charge level can be maintained by a separate charging device, and significant improvement in performance can again be obtained.

When a precharging device is used, the paths of the dust particles as they approach the fabric are altered so that dust collection occurs preferentially on the electrodes and near the bag entrance. Measurements show that the dust mass redistribution over the surface of a bag accounts for a large part of the reduction in pressure drop. Calculated particle trajectories are consistent with the observed pattern of dust deposition on the bag wall, but also indicate a region with radius equal to half the bag radius in which the electric field strength is almost zero and in which particles respond only to the flow field.

Besides responding to changes in dust mass distribution, pressure drop is also reduced because of the higher permeability of a dust cake formed in a strong electric field. The relative importance of the two effects varies as the dust is more or less uniformly distributed over the bag surface. The increased permeability is largely due to a shift upstream into a region of the fabric having lower solidity. This has been demonstrated experimentally, and mathematical modeling shows that the pressure drop is also sensitive to whether the dust collects as dendrites or as compact coatings on the fibers. Agreement between models and experimental results requires assumption of an intermediate mode, expressed as the dendrite fraction. Experimental determination of this fraction has not been accomplished.

There is no benefit to be derived from programming the voltage applied either to the bag electrodes or to the precharger. Sudden reversal of the voltage polarity when the bag is cleaned gives negligible improvements in cleaning. Use of AC rather than DC potentials resulted in slightly higher pressure drops, higher penetrations, and large electrode currents. However, although improvements in performance with AC were smaller than with DC, it is worth noting that use of AC in ESFF need not be ruled out.

As face velocity is increased, performance depends increasingly on cleaning energy. High cleaning energy, as in pulse-jet cleaning, leads to large penetration, while pressure drop remains within a commercially acceptable range. Low cleaning energy, as in reverse air with shaking, leads to large pressure drop, with penetration remaining low. Shear cleaning, a method which uses in-plane shear deformation of the fabric to aid reverse air cleaning, appears to have some potential as a nontraumatic substitute for shaking.

"Printed" electrodes, i.e., bands of conducting material deposited on the filter fabric, are as effective as wires in producing ESFF. Their use by utilities depends on finding a formulation for the material that will resist the temperature and chemical environment of the baghouses.

SECTION 3

RECOMMENDATIONS

Electrode systems should be designed so as to maximize field intensities and particle charge levels. Replacing the lightning rod with an axial wire for corona charging should achieve both ends. For pulse-jet baghouses, the wires would be suspended between the bags.

To maximize electric effects, the highest voltages should be used. This, however, may lead to problems analogous to the back corona experienced with electrostatic precipitators. The possible occurrence of this type of phenomenon should be studied, as well as means for preventing it.

Fabrics having an upstream region of low solidity should be developed that are suitable for commercial production and for the fabrication of bags. Bags made of these fabrics should undergo tests to determine long-term performance.

Conducting substances to be used for printed electrodes should be formulated so as to withstand baghouse conditions. Bags with electrodes made of these materials should then be tested in a pilot plant.

The potential usefulness of shear cleaning should be further investigated, including its effects on penetration and bag life.

SECTION 4

EFFECTS OF PARTICLE CHARGE LEVELS

LIGHTNING ROD PRECHARGER

When wire electrodes were embedded in a fabric for ESFF, the response of filtration performance to an applied voltage often decayed (or "faded") with time, until, in some cases, the pressure drop was actually higher with an applied field than without it. The problem occurred with either pulse-jet or reverse air cleaning and with both woven glass and Teflon® felt bags. It was so severe that at one time the prospects for successful development of ESFF appeared rather poor. It was suspected that fading was due to the suppression of corona discharge by the dust cake. The specific charge of the fly ash aerosol used in the TRI baghouse is very low, and it had been shown that in order to obtain substantial pressure drop reductions, it was necessary to raise the potential on the electrodes to above the corona threshold value [3]. Thus the electrode wires acted both as aerosol prechargers and as means for providing the electric field for polarizing the fibers in the filter fabric. With pulse-jet cleaning, the problem was solved (and the above hypothesis supported) by the finding that if the electrodes were not stitched into the fabric, but instead supported by a separate "harness" that held them close to the upstream surface, fading was completely eliminated. This was assumed to result from slight movements of wires relative to the fabric when the bag was pulsed, which kept dust from accumulating on the wires. Such a solution was not possible with reverse air bags, since, in order to be on the upstream side of the fabric, the electrodes had to be on the inner surface of such bags, rendering impossible the use of a harness.

On the basis of the above hypothesis, it was assumed that it should be possible to eliminate fading by using a separate precharger. To test this, an experiment was designed using a woven glass reverse air bag (J.P. Stevens type 648 fabric) having 150-μm wire electrodes stitched in at a stitch frequency of 4 per inch, a condition that caused fading previously. The precharger was a metal rod with a few short pieces of fine wire attached to the end, so as to resemble a lightning rod. It was located near the entrance to the bag, as in Figure 1, the intention being to ensure that all the charged dust would enter the bag.

Measurements were made at two face velocities using different bag and precharger voltages, and the results are shown in Figure 2. It can be seen that with a combination of precharger and bag electrodes, very low values of

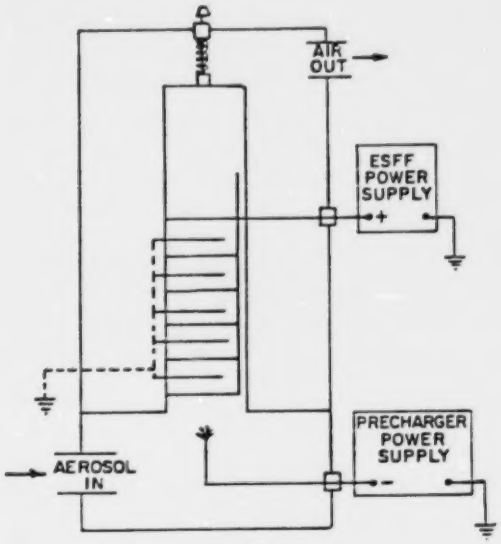

Figure 1. Location of "lightning rod" precharger in reverse air baghouse.

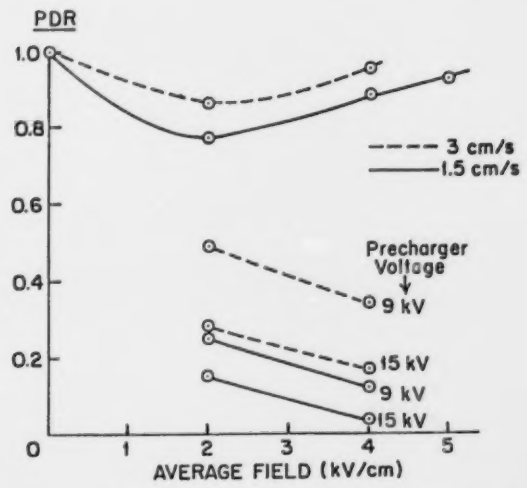

Figure 2. Dependence of PDR on bag field after extended run for a woven glass reverse air bag. Top curves: no precharger.

pressure drop ratio (PDR) were obtained. (The quantity PDR is the ratio of the pressure drop buildup during a filtering/cleaning cycle when electric stimulation is applied to the corresponding pressure drop buildup without the applied field.) These were also clearly dependent on face velocity. It can also be seen that without precharging (top two curves), the curves show minima typical of fading behavior.

Similar measurements were made to test the efficacy of precharging in suppressing fading with pulse-jet cleaning. The baghouse was converted to pulse-jet operation, and a new bag (also made of J.P. Stevens type 648 woven glass) was fitted with 150-μm wire electrodes on the outer surface, this time at a frequency of one stitch per 3/4 inch. The baghouse was run at a face velocity of 15 mm/s (3 ft/min) and cleaned off-line (i.e., with the main flow off). The intention was to approximate conditions previously found to cause fading and to investigate the effectiveness of the precharger in offsetting it. The shape of the charger was modified to suit the air flow pattern, i.e., it was made in the form of a ring with fine wires protruding outwardly all around.

As can be seen in Figure 3, the PDR under these conditions remained at 0.6 until about the 70th cycle, and then rose to about 0.85, as fading set in. PDR values for the next 40 cycles fluctuated between 0.83 and 0.90. At cycle 110 application of voltages of 9 and 15 kV to the precharger resulted in large reductions in PDR. Thus, use of the precharger appears to be as effective with pulse-jet operation as with reverse air.

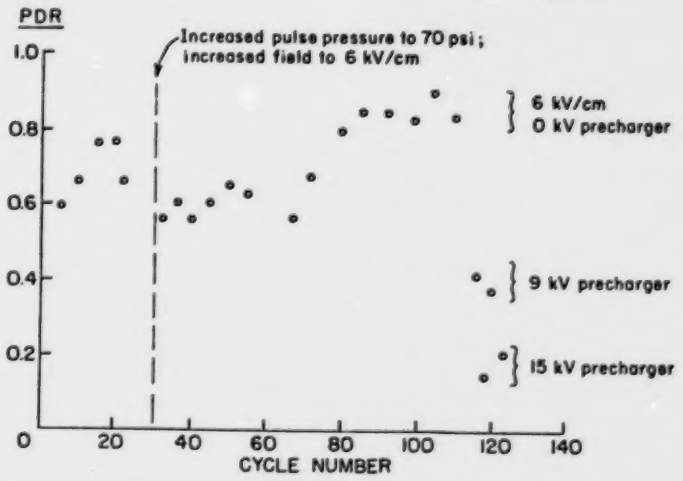

Figure 3. ESFF fading with a woven glass pulse-jet bag, and recovery of low PDR by using the precharger.

With this configuration, however, the mechanism of pressure drop reduction is not as clear as with reverse air, since it is likely that an unknown fraction of the charged inlet dust is driven to the walls of the baghouse. Thus the relative contributions to the pressure drop reduction of the charging and of the loss of inlet dust cannot be assessed precisely.

These results support the view that a minimum level of particle charge is necessary for satisfactory ESFF operation. In this context, results of the tests in the first pilot plant (in Waynesboro, VA) were pertinent [4]. These tests were run without precharging and with electrodes that were on the downstream side of the bag, so that no precharging by the electrodes was possible. Yet no fading was experienced. Although it is difficult to make direct comparisons, it also appears that PDR values obtained at Waynesboro were lower than those at TRI. At Waynesboro, PDR values of 0.6 were obtained at 2.2 kV/cm and 3 ft/min, with reverse air cleaning, while at TRI under comparable conditions, the PDR was about 0.8. There appears to be, therefore, a strong possibility that the dust processed at Waynesboro had a higher charge level than the TRI dust. Similar considerations apply to the pilot test at the Southwestern Public Service Harrington Station at Amarillo, TX, where fading was also not experienced.

The rather low PDR values shown in Figure 2 prompted further measurements with precharged aerosols. A third set was made with a Teflon nonwoven felt bag cleaned by reverse air with shaking and fitted with printed electrodes. Printed electrodes (PE) are discussed in greater detail in a separate section. In the present case they served to show that the combination of precharging and bag electrodes functioned as well with PE as with wire electrodes. The results, in Table 1, show that smaller PDR values are obtained if the precharger potential and that on the bag electrodes are of opposite polarity. It is also interesting to note that in this case, precharging alone gave a negligible reduction in pressure drop.

TABLE 1. PRESSURE DROP RATIOS WITH ESFF AND PRECHARGED AEROSOL
(Teflon® bag with PE. Inlet concentration 4.8g/m^3. Face velocity 3 cm/s.)

Bag field (kV/cm)	Precharger voltage (kV)	$\Delta P_i / \Delta P_f$ (mm H_2O)	PDR
0	0	16/110	
0	-9	16/107	0.97
+2	0	15/83	0.67
+2	-3	14/60	0.45
+2	-6	14/40	0.25
+2	-9	14/28	0.14
-2	0	15/60	0.43
-2	-3	15/57	0.41
-2	-6	15/56	0.40
-2	-9	15/41	0.26
-3	0	15/52	0.36
-3	-3	15/52	0.36
-3	-6	15/46	0.31
-3	-9	15/35	0.19
+2	+9	16/39	0.22
-2	+9	17/31	0.13

MECHANISMS OF PRESSURE DROP REDUCTION

To study the mechanism by which precharging reduces pressure drop, the bag support was modified to allow the bag to be removed easily from the baghouse. A new textured woven glass bag with stitched-in 150-μm wire electrodes was made. The sewn seam of the bag was replaced with an overlap held closed by clamps. With this arrangement, the bag (after being removed from the baghouse) could be carefully opened so the dust cake could be examined. Visual inspection immediately showed that nonuniform distribution of the dust deposit occurred in both the longitudinal and tangential directions. Deposition was heavier at the lower end of the bag and on the electrodes, as shown in Figure 4.

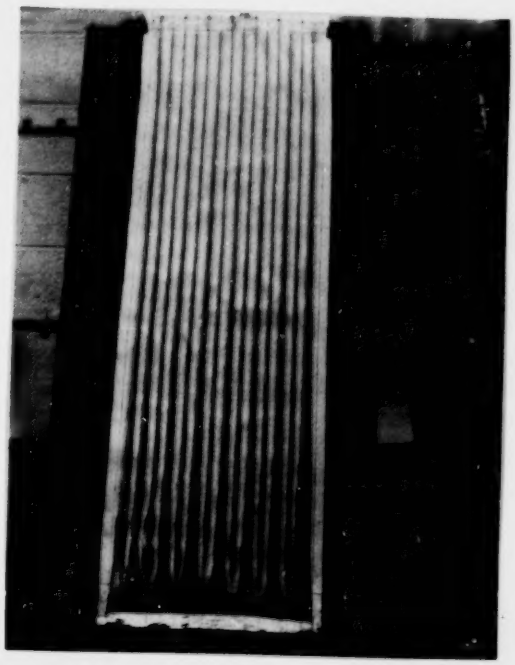

Figure 4. Dust deposition pattern with 4 kV/cm field and -15 kV precharger potential.

Mass distribution with respect to bag height was measured by placing a mask at a series of positions over the opened bag and aspirating the dust from the area within the mask. The dust was collected on a filter and weighed. The results for various combinations of bag fields and precharger potentials are plotted in Figure 5: in all cases more dust collects at the bottom than at

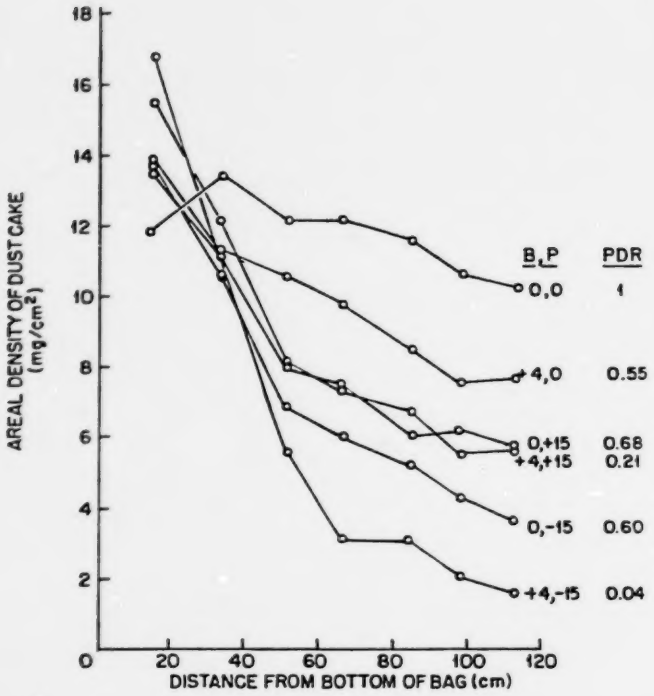

Figure 5. Distribution of dust mass with respect to distance from the bottom of the bag. B and P indicate average field on bag in kV/cm and voltage on precharger in kV, respectively.

the top of the bag. When this occurs with no voltage applied, the cause is assumed to be settling by gravity, but with an applied field, the tendency for early deposition is increased. Values of PDR are listed alongside the curves. It should be noted that these were values obtained from the pressure drop reached after 15 minutes, starting from an almost clean bag. The bag was cleaned by vacuuming each time so as to allow measurement of the dust deposit areal densities plotted in Figure 5. Although the PDRs in Figure 5 must therefore not be regarded as typical of values that would be obtained after prolonged conditioning, they nevertheless bear a certain relationship to the curves. It can be seen that curves with greater slopes tend to correspond to lower PDR. Deviations from this trend must be attributed to nonuniformity in distribution in a tangential direction, clearly seen in Figure 4, which is a photograph of

the opened bag after being run 15 minutes with an average +4 kV/cm field between wires and a -15 kV potential on the precharger (+4,-15). It can be seen that: (1) Most of the dust collects on the positive wires. (2) The amount collected, as plotted in Figure 5, is greatest at the bottom and diminishes with distance up the bag. (3) Some collection occurs on the ground wires; this may be dust that, having deposited on the positive wires, is reentrained after gaining a positive charge. (4) Spaces between wires are left essentially clean.

Photographs taken of the bag surface and dust deposits are shown in Figures 6, 7, and 8. In all these photographs, pieces of adhesive tape had been stuck to the clean bag over portions of some of the electrodes. The patterns of dust deposition on the tape lead to some interesting conclusions about the motion of dust particles during filtration: Figure 6 shows the bag surface after vacuuming (a) and with a dust cake laid at no applied voltage (b). No dust has collected on the pieces of adhesive tape because there is no air flow normal to the tape. Figure 7 shows dust deposited with a 4 kV/cm field between bag electrodes and +15 kV (a) and -15 kV (b) on the precharger. In both cases the dust forms visible bands on the wires, but the bands are sharper when bag voltage and precharger voltage are of opposite sign. An interesting feature of this figure is that dust was deposited on the adhesive tape in an amount apparently equal to that elsewhere on the band. This indicates that particle velocities due to the field near the wires are much greater than the gas velocity. The bag is thus acting like a precipitator. Figure 8 shows the appearance of the dust deposits when only a bag potential was applied. Here there are still visible bands, but they are more diffuse and dust is again deposited on both the electrodes and the adhesive tapes. When only the precharger was activated (b and c), the dust deposit was uniform, and there was some deposition on the tapes, presumably of dust driven to the wall by space charge effects.

After each of the 15-minute runs specified in Figure 5, the bag was weighed and the mass of dust determined. Table 2 shows that no matter what the combination of bag and charger potential, the mass collected in 15 minutes was always the same. Thus the changes in pressure drop were not to any extent due to reduced total dust loading. This appears to disagree with the data in Figure 5. In that figure the total mass of dust should be proportional to the area under each curve, and the lower curves appear to enclose smaller areas. The explanation must be that the sharp upswings to the left of the lower curves were plotted with too few points to show accurately the amount in those regions. Figure 4 shows that heavy deposition occurs within a few centimeters of the bottom of the bag; the telephone (12 cm high) to the right of the photograph gives an idea of scale.

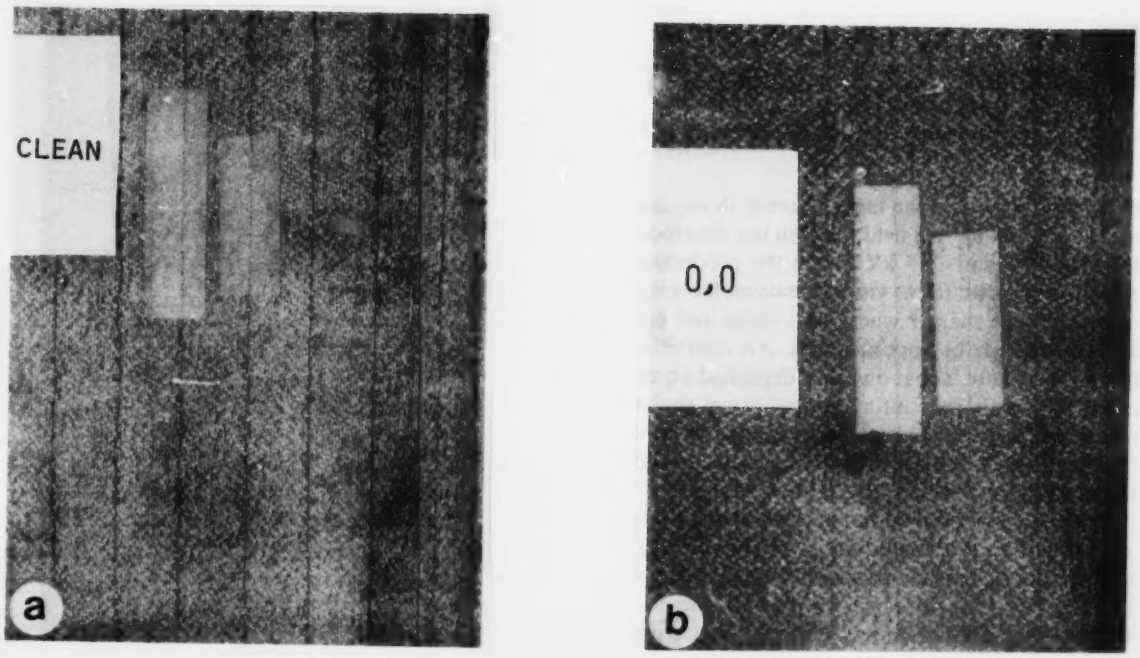

Figure 6. Appearance of the inner surface of the bag:

a) after vacuum cleaning through a wire screen.
b) with an average of 7.5 mg/cm^2 of fly ash deposited with no electric field or precharging.

No fly ash has deposited on the tape in either case. In Figures 6, 7, and 8, horizontal bands are due to anticollapse rings inside the bag.

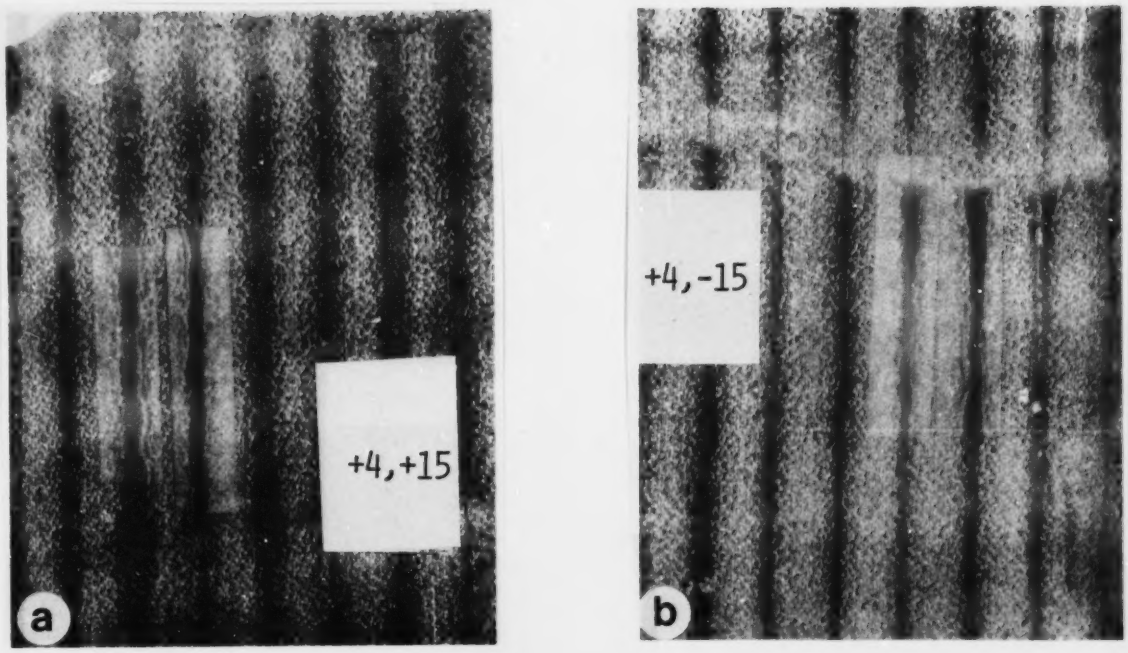

Figure 7. Appearance of the inner surface of the bag:

a) after deposition with 4 kV/cm between bag electrodes and +15 kV on the precharger.
b) after deposition with 4 kV/cm between bag electrodes and -15 kV on the precharger.

Points to note: (1) Dust collects on tape. (2) Bands are narrower with negative precharging.

Reproduced from
best available copy.

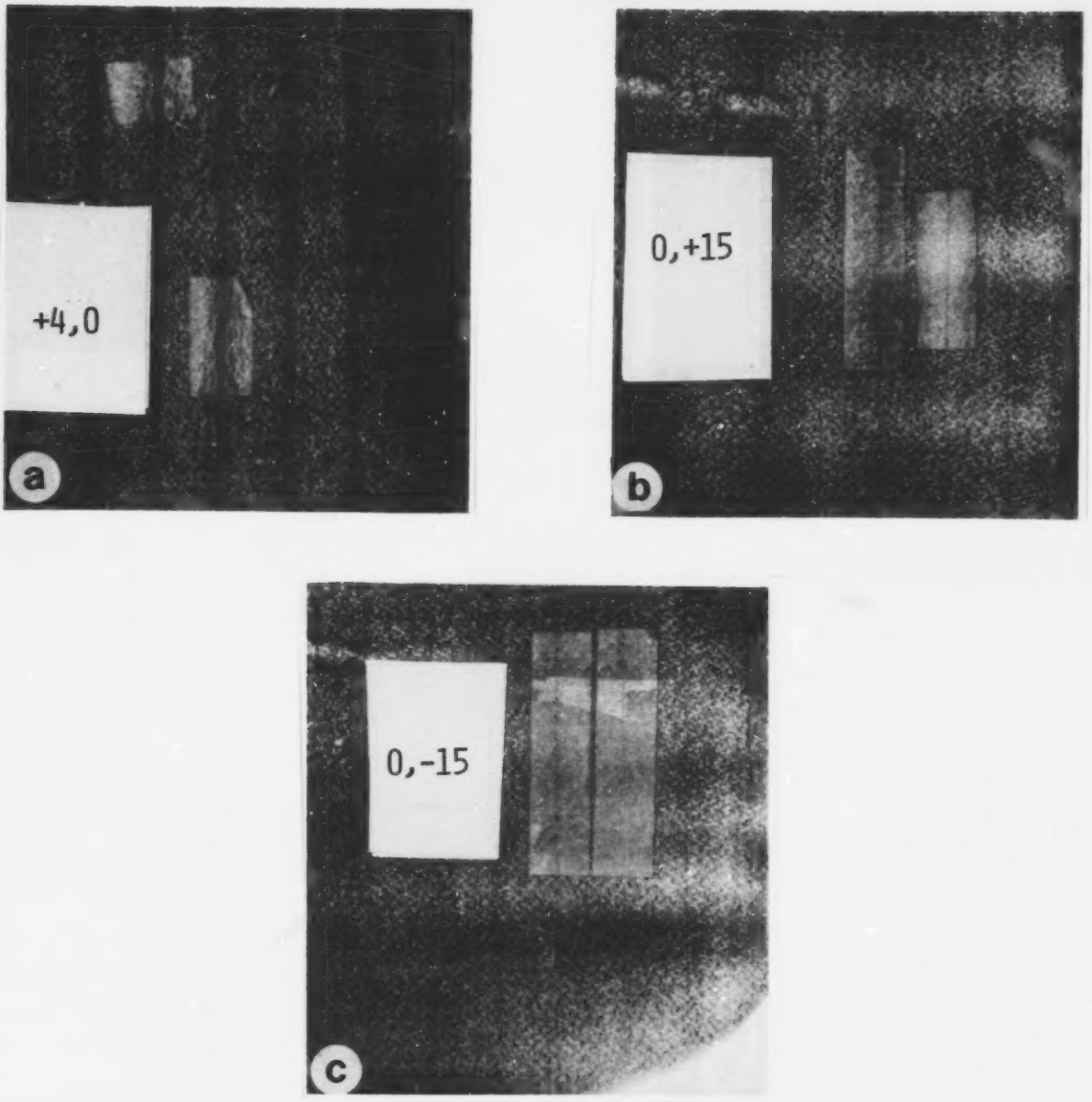

Figure 8. Appearance of the inner surface of the bag:

a) after deposition with 4 kV/cm between bag electrodes and no precharging. Dust deposits in bands on both sets of electrodes and on tapes.

b) with positive precharging only. Faint bands are visible on grounded electrodes, including area covered by tape.

c) with negative precharging only. No bands are visible.

TABLE 2. MASS OF DUST COLLECTED ON BAG IN 15 MINUTES

Bag field (kV/cm)	Charger voltage (kV)	Mass of dust collected (g) in two trials
0	0	30, 31
+4	0	33, 31
+4	-15	27, 29
+4	+15	37, -
0	-15	35, 27
0	+15	32, 31

Any technique capable of reducing pressure drop offers several possible benefits: one can choose to operate at a lower energy consumption level, allow longer intervals between cleanings, or, by raising face velocities, use fewer bags. A recent study [9] has shown that the third of these options gives the largest savings in operating costs, and it may be assumed that in any future commercial development of ESFF, face velocities will be higher than those in present practice. However, limits to face velocity are imposed by falling efficiency. The possible increases in face velocities attainable in the combined bag electrode/precharger mode were explored by making measurements of efficiency at a series of velocities using the same textured woven glass bag as in Figures 4 through 8. Figure 9 shows efficiencies obtained with no field (0,0), with +4 kV/cm average field between electrodes (+4,0), and with +4 kV/cm between electrodes and -15 kV on the precharger (+4,-15). There is a clear enhancement of efficiency at all velocities by ESFF, especially with precharging. Long-term tests in a pilot plant will be needed to determine the maximum velocity at which stable operation is possible. Results appearing in Section 5 support the low penetration results in Figure 9 (cf. Figure 34) but show that with reverse air cleaning, pressure drop rises out of control. Finding the proper method for cleaning the bag is thus essential to successful ESFF operation at higher face velocities. It is reasonable to assume, however, that with a precharger/electrified bag combination, appreciable increases in face velocity will be possible.

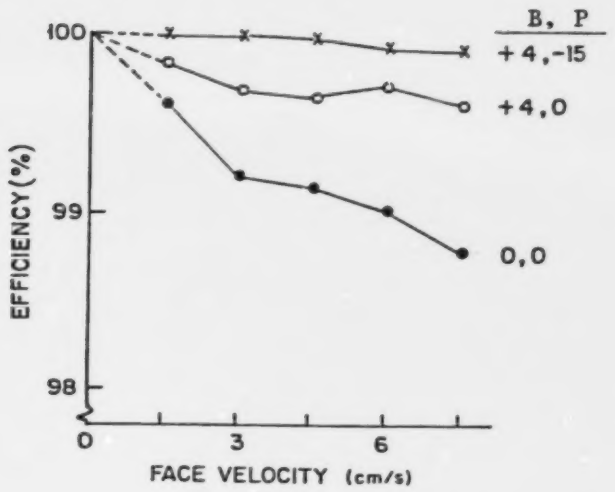

Figure 9. Dependence of efficiency on face velocity for woven glass bag with and without ESFF. B and P indicate the same quantities as in Figure 5.

For two conditions, (+4,+15) and (+4,-15), tangential as well as longitudinal dust mass distributions were measured by aspirating dust from 8 mm x 120 mm areas on the positive and ground wires and from the space between, at each of 5 distances from the bottom of the bag. The dust cake areal densities for the 15 representative bag locations, shown in Table 3, show the same shift towards the bottom of the bag seen in Figure 5. However, the distribution of dust mass with respect to the electrodes is somewhat different from what might be expected. In the case (+4,-15) where the dust has been given a negative charge, there is a clear preponderence of collection on the positive electrode. (The substantial amount that collects on the ground electrode has been assumed to be dust that, being first collected at the positive wire, acquires a positive charge and is then reentrained. This hypothesis is supported by the fact that the fraction of the total dust deposited that collects on the ground wire is greater at the bag top than at the bottom.) In the case (+4,+15) where the dust was charged positively, however, the expected preferential deposition on the ground wire is not seen. In both cases, the amount between wires is small, especially for the (+4,-15) case.

TABLE 3. DISTRIBUTION OF DUST AREAL DENSITIES (mg/cm^2) ON REVERSE AIR BAG ON POSITIVE, GROUND, AND BETWEEN ELECTRODE WIRES

Distance up bag (cm)	(0,0)[a]			(+4,+15)[a]			(+4,-15)[a]		
	Pos. wire	Ground wire	Betw. wires	Pos. wire	Ground wire	Betw. wires	Pos. wire	Ground wire	Betw. wires
20	12.2	12.2	12.2	7.02	5.76	2.03	13.57	1.87	0.16
40	13.0	13.0	13.0	3.16	6.44	3.05	6.26	2.67	0.28
60	12.2	12.2	12.2	3.95	3.00	0.75	2.46	1.76	0.15
80	11.8	11.8	11.8	1.82	3.15	1.93	1.63	1.26	0.11
100	10.9	10.9	10.9	2.14	2.92	0.53	1.10	0.84	0.07
$R^b = [\Sigma \frac{1}{R_i}]^{-1}$		0.80			0.13			0.022	
PDR[c] (calc)					0.16			0.028	
PDR[c] (meas)					0.21			0.040	

[a] First numeral = potential gradient between electrodes (kV/cm).
Second numeral = potential on precharger (kV).

[b] R = total resistance to air flow; R_i = air flow resistance of area i.

[c] PDR = pressure drop ratio = ratio of pressure drop with applied field and precharging to that without either.

The resistance R to air flow for the entire bag was calculated assuming that the resistance R_i for each small area was linearly proportional to the areal density of dust deposit, and that, in analogy with the rule for electrical resistances,

$$R = [\Sigma \frac{1}{R_i}]^{-1} .$$

Values of PDR, or pressure drop ratio, calculated as the ratio of the R values determined for the electrified cases to R for the (0,0) case are compared in Table 3 to the measured PDR values. The degree of agreement obtained indicates that the reductions in pressure drop due to bag electrification and precharging under the conditions of these experiments can in large measure be explained by dust redistribution.

PERMEABILITY SCANNING

Pressure drop reductions observed with electrically stimulated fabric filtration (ESFF) are commonly attributed to two different factors: increased porosity of the dust cake and nonuniform dust deposition. The latter mechanism is analyzed in the previous section, and supported by Chiang et al. [5] as the primary reason for pressure drop reduction. A simple permeability scanning experiment was devised to discriminate between the two mechanisms. The method consisted of depositing a fly ash dust cake on a bag (6 ft/min, 15 min filtering, 32 g total deposition), then opening the bag flat. A metal tube of 0.5 cm i.d. was connected to a source of compressed air and the flow from the tube adjusted so that the air velocity was 3 cm/s (6 ft/min); the calibration was made with a bubble flowmeter. The end of the tube was pressed against the dust cake at 15 tightly spaced locations spanning three adjacent electrodes. Arrangements were made to ensure a good seal so that the excess pressure in the tube (measured by a manometer) was the full pressure drop needed to drive the air through the small area of dust cake covered by the tube. In this way the distribution of dust cake permeability around the electrode wires was mapped for the filtering conditions (+4,-15). The results are plotted in Figure 10.

Several features of these plots are notable. One is the discrepancy between the plotted points and the pressure drop for the bag, indicated as a double horizontal line. This was probably due to the pressure that must be exerted on the fabric to effect a seal around the scanner tube. The compressed fabric should have a lower permeability, and this is reflected in the estimated 4 mm of water increase over the bag pressure. Differences in cake permeability at different locations should not be affected by this compression.

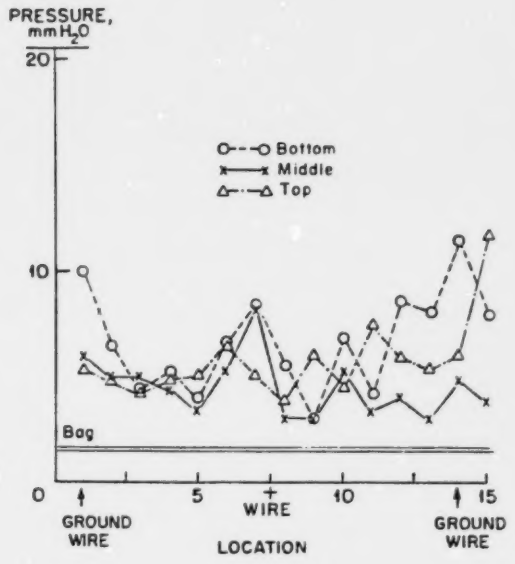

Figure 10. Permeability of dust cake deposited with (+4,-15) at various filter bag locations and for the bag as a whole (double line).

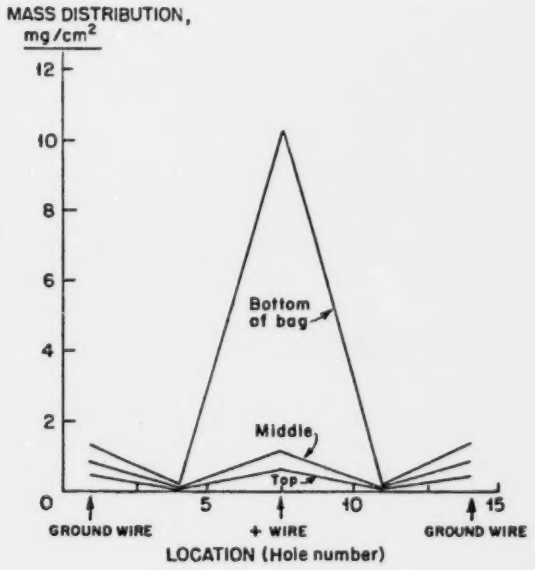

Figure 11. Dust cake mass deposited with (+4,-15) at various locations on the inner surface of the filter bag.

The second, more meaningful feature of the plots is the difference between the permeability patterns and those expected from the visual appearance and measured mass distribution of the dust cake. Figure 10 clearly shows the variations of pressure drop with dust deposition, but the relative heights of the maxima and minima do not match the pattern in Figure 11 which shows the mass distributions. It can be seen that although the mass collected on the positive wires is several times greater than on the ground wires, the pressure peak is lower on the positive wires. Again, although the mass on the positive wire at the bottom of the bag is much larger than at the top, the pressure drop at these two locations (and at the middle) do not show the same relationship. Lastly, the mass collected at the bottom of the bag is greater for (+4,-15) than for (0,0), but even on the positive wires where the heaviest deposition occurred, the pressure drop at (+4,-15) does not exceed that at (0,0) which is nowhere less than 15 mm of water.

All these facts point to strong differences in dust cake structure and permeability depending on the conditions of deposition. In particular, the dust cake formed with a strong electric field is much more permeable than without the field. These results appear to be in disagreement with the findings of the preceding section which indicated that reductions in pressure drop were chiefly due to dust cake redistribution, but in fact the two sets of results need not be inconsistent because the resistance of a number of resistors in parallel is controlled by the lowest. Thus once pressure drop is reduced by establishing a pattern of thick and thin dust cake regions, any increase in the porosity of the thick regions makes only a small difference in the total resistance. In any case, from these results it may be concluded that pressure drop is reduced by both redistribution and by increased dust cake porosity, but that the first effect is the dominant one under the conditions studied.

ELECTRIC FIELD AND PARTICLE TRAJECTORIES IN AN ESFF BAG

In order to explain the observed patterns of dust deposition in the filter bag in terms of the electrical forces that give rise to them, some knowledge of the shape and strength of the electric field and of the particle charge was needed. These could then be used to compute particle trajectories and locations where the dust would deposit. This section gives an account of experiments and computations designed to obtain this information.

A Faraday cage was mounted on the outer wall of the baghouse, fed by a pipe which pointed into the tube sheet opening as illustrated in Figure 12. It consisted of a filter on which the dust collected, backed by a porous metal plate connected to a Keithley electrometer. Charges on the dust leaked to the metal plate and to the electrometer, which measured the leakage current.

To make the measurements, the baghouse was run without a bag, so that when all the systems, including the precharger, were turned on, a stream of charged fly ash aerosol came through the hole in the tube sheet. Isokinetic one-minute samples of the dust on the Faraday cage filter were weighed, and the

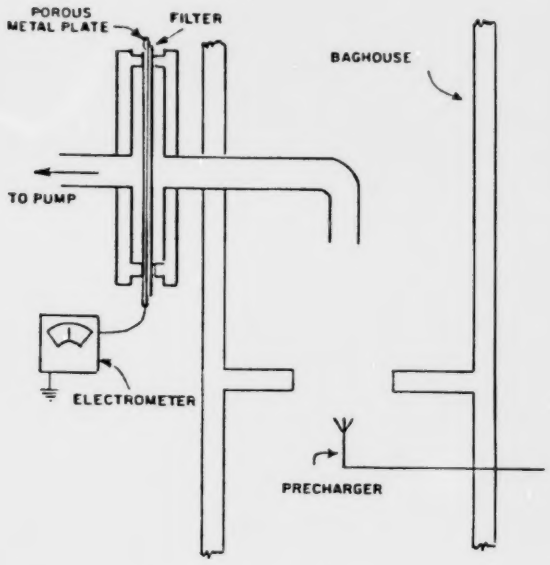

Figure 12. Faraday cage for the measurement of particle charge due to precharging.

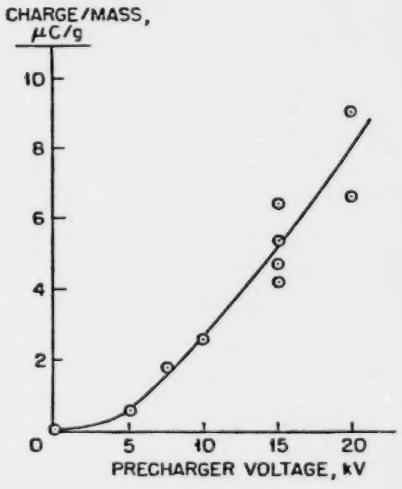

Figure 13. Charge/mass ratio as a function of precharger voltage for a fly ash aerosol stream.

corresponding electrometer current readings recorded. The resulting charge/mass values are plotted in Figure 13. They are slightly larger than values obtained by Donovan et al. [6], probably because of differences in the experimental arrangements and in the fly ash used.

The object of measuring charge/mass ratios, q/m, is to assign values of this parameter to various particle size ranges. Ideally, q/m ratios should be measured for each size range, but since this is significantly more difficult, the assumption was made that particle charge is proportional to particle surface area. On this basis, the average charge of 5 μC/g obtained with a precharger potential of 15 kV (Figure 13) was distributed as shown in Figure 14. The mass fraction in each size range had previously been determined, the size ranges corresponding to those captured on the stages of an AIR impactor (Aerostatics Instrumentation & Research, Logan, Utah).

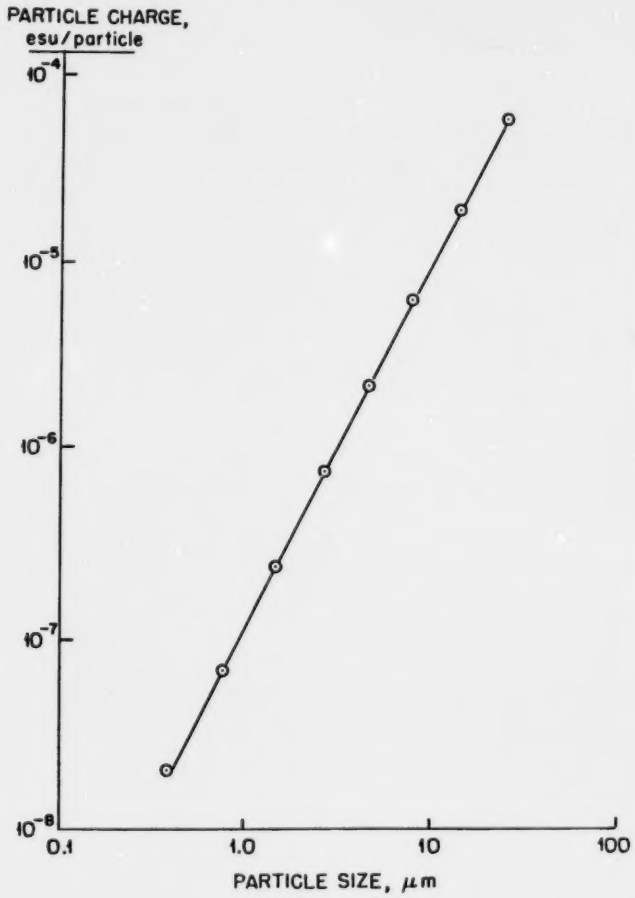

Figure 14. Particle charge as a function of particle size.

The approximate theoretical maximum charge q_p acquired by a particle of diameter d is given by [7]

$$q_p = 0.75\ Ed^2,$$

where E is the field near the particle, and all units are cgs and esu. The value to be assigned to E in the present case is uncertain, since, as it passes the precharger, a particle travels through regions of different field intensity. It follows that particle charge levels would depend not only on their size but also on how close they pass to the charger. However, some self-leveling mechanisms may be provided by the fact that particles in a high field region quickly move away from the charger to a region of lower field. This should narrow considerably the spread of charge levels for each particle size. These considerations mean that the relationship in Figure 14, though valid, can only be taken to give average values of charge and that in fact the line in that figure occupies the center of a band of unknown width. The particle trajectories calculated later in this section must consequently also be rendered more diffuse.

The electric field inside a bag fitted with electrodes is due to the charge which appears on the electrodes when a potential is applied to them. The field E at a distance r from a straight wire carrying a charge q per unit length is

$$E = \frac{2q}{r} .$$

If a number of electrodes are involved, the field will be the vector sum of all contributions. In the case considered here, the electrodes are parallel to the bag axis and are alternately grounded and raised to a high potential. The problem then is to find the charge on each wire. An analysis for one pair of parallel wires is available [8], but extension of the treatment to cover nonplanar arrays of more than two wires was not attempted.

A more direct approach was taken - namely, experimental measurement of the capacitance of wire arrays. The instrument used was a bridge-type capacitance meter (General Radio Co. Type 740). The meter was tested against a number of known capacitors ranging from 10^{-5} to 10^{2} μF, and the measured values were found to match the rated capacitances within roughly 10%; the capacitors themselves do not have a guaranteed accuracy much better than this.

The capacitance C of two parallel cylindrical conductors of radius a, separated by a distance b, is given by

$$C = \frac{k}{2 \ln \left[\dfrac{b + \sqrt{b^2-4a^2}}{b - \sqrt{b^2-4a^2}} \right]} \text{ esu/cm},$$

where k is the dielectric constant of the medium between the conductors, which is roughly unity for air. A straight cylindrical conductor of radius a held horizontally a distance h above an infinite grounded plane also has a capacitance-to-ground C_g given by

$$C_g = \frac{k}{2 \ln \left[\frac{h + \sqrt{h^2 - a^2}}{a} \right]} .$$

When the diameter of the conductors is 0.025 cm and their length 11 m, C is 6×10^{-5} μF. If the distance h is 2 m, C_g is likewise 6×10^{-5} μF. In practice, both effects operate simultaneously, but because of interference, the total capacitance is less than the sum of C and C_g. Nevertheless, it can be shown (D. Myers, Princeton University, personal communication, 1984) that the ratio of the charge carried by the positive wire to that on the grounded wire differs negligibly from 2, so that the capacitance of the system is still effectively the sum of two equal capacitances, allowing the charge distribution shown in Figure 15.

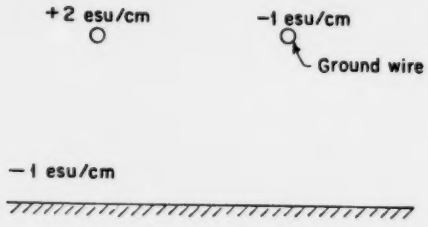

Figure 15. Charge distribution assumed for calculations leading to trajectories in Figures 16, 17, and 18.

The capacitance of a model electrode system was then measured. A cage was built by stringing 18 alternately coupled parallel wires between two plexiglass disks, 1.22 m apart, to form a cylindrical array; the distance between wires was 2 cm. The spacing was identical with that of the electrodes in the bag shown in Figure 4. As in the bag, alternate wires were grounded and the others connected to the positive terminal of the capacitance meter. The cage wires were equivalent to a pair of wires 11 m long. The capacitance of the cage was found to be 7.8×10^{-5} μF, or 70 esu. When the potential difference between wires is 9 kV, or 30 esu of potential, the total charge is 2100 esu and the charge per unit length of wire is thus ∿2 esu/cm. The capacitance of a pair of straight wires 11 m long was also measured and found to be 7.2×10^{-5} μF, or, within experimental error, almost equal to that of the cage.

The charge per unit length just obtained and the specific charges plotted in Figure 14 were now used to plot particle trajectories within a bag. A computer program was written that summed the x and y components of the field due to the charge on each of the 18 electrodes at a point in the bag. From this and the charge and size of a particle near the bag axis, the particle velocity was calculated, and hence its position 0.1 s later. The calculation was repeated starting from this new point, and stopped when the particle reached the bag wall. A face velocity of 3 cm/s was assumed, which gave the particle a basic radial velocity of 3R/5.8 cm/s, where R was the radial position of the particle and the bag radius was 5.8 cm. Such calculations were made for 1, 3, and 10 μm particles, which had q/d ratios of 1.5×10^{-3}, 3.33×10^{-3}, and 11.2×10^{-3} esu/cm, respectively.

The computed trajectories shown in Figures 16, 17, and 18 can be seen to predict the kind of deposition pattern actually observed in Figure 4. The figures show trajectories in only 2 of the 18 sectors of the horizontal section through a bag, the sectors bounded by radii passing through the electrodes. Because of symmetry, the behavior in all other sectors would be identical. The particles are assumed to start near the center of the bag and to travel toward the bag wall at a speed which, in the absence of electrical effects, would increase with radial position so as to be zero at the center, 3 cm/s at the bag wall, and 3R/5.8 cm/s at a distance R from the center. In the absence of electrical effects, the particles would follow radial paths. The figures illustrate the deviations from these patterns when a nominal 4.5 kV/cm field is applied. The larger (negative) particles are sharply deflected in the direction of the positive electrode and make a direct hit on the electrode no matter what the starting point. This is not true of the smaller particles; they collect in a narrow band near the electrode.

Radial field intensities on the radii at the sector boundaries are plotted in Figure 19. It is interesting to note how at radial positions as far from the center as half the bag radius, the intensities are near zero. This accounts for the appearance of the trajectories in Figures 16, 17, and 18, which begin to deviate from radial directions only when the particle moves beyond half the bag radius. Greater improvements in performance should be expected, therefore, with an electrode system that generated a strong field in this central region also.

Velocities of particles moving along these sector boundary radii are plotted in Figure 20. For these particles, the symmetry of the field causes radial acceleration only. Here it can be seen that the particles approaching a positive electrode (top three curves) are accelerated to rather high velocities, but those traveling toward a ground electrode (lower three curves) slow down and stop at a distance that depends on the q/d value for the particle.

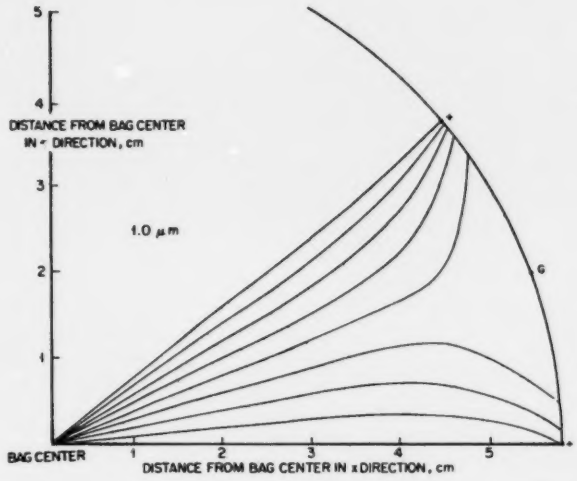

Figure 16. Trajectories of particles 1 μm in diameter with $q/d = 1.15 \times 10^{-3}$ esu/cm.

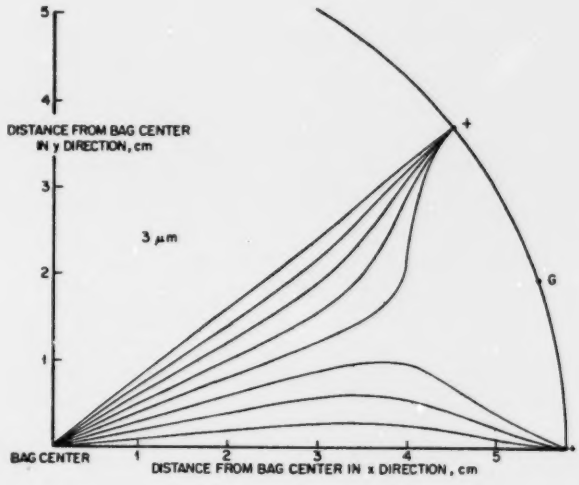

Figure 17. Trajectories of particles 3 μm in diameter with $q/d = 3.3 \times 10^{-3}$ esu/cm.

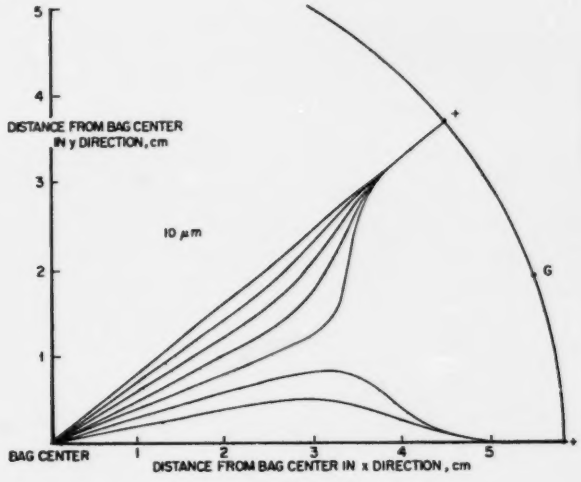

Figure 18. Trajectories of particles 10 μm in diameter with $q/d = 1.12 \times 10^{-3}$ esu/cm.

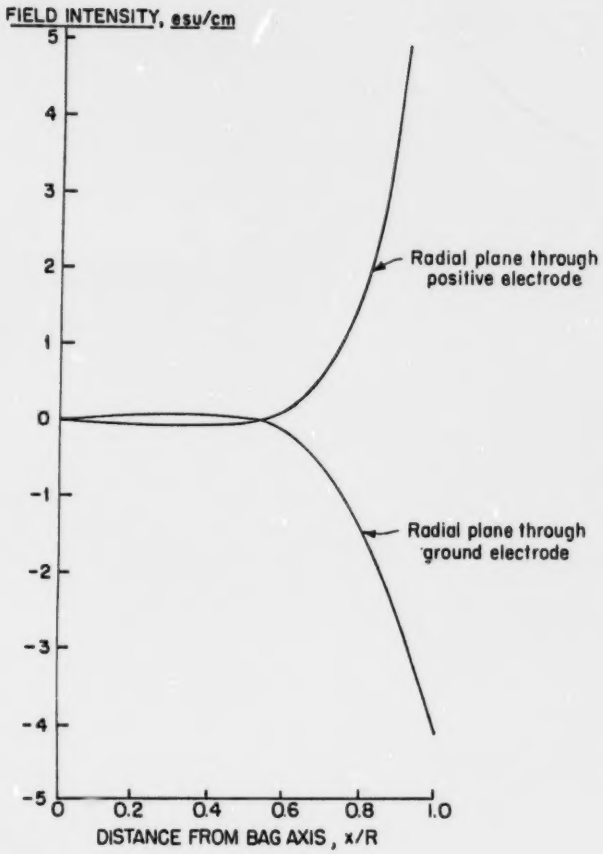

Figure 19. Field intensity on radial planes passing through the electrodes.

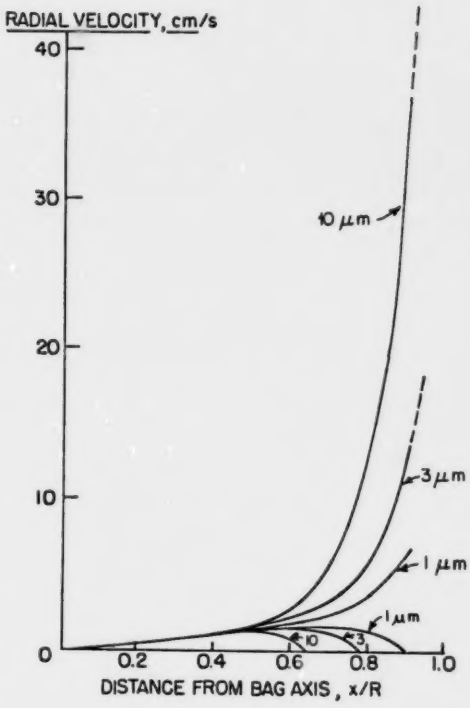

Figure 20. Radial velocities for particles of indicated diameters moving in radial planes through electrodes.

Upper 3 curves: plane through positive electrode.

Lower 3 curves: plane through ground electrode.

PARTICLE SIZE DISTRIBUTION AS A FUNCTION OF LOCATION IN AN ESFF BAG

The dependence of specific charge on particle size discussed above implies different velocities for particles of different size. The velocity v of a particle with diameter d moving in air under a force F is given by

$$v = \frac{F}{3\pi\eta d} ,$$

where η is the viscosity of air. If the force is coulombic and is due to an electric field E acting on the particle charge q, and q is proportional to particle surface area ($q \propto \pi d^2$), then

$$v = \frac{KE}{\eta} d ,$$

so that v varies directly as the particle diameter. In a baghouse with ESFF, one would therefore expect the larger particles to be collected closer to the entrance.

To see whether this actually occurred, particle size distributions were measured at various locations on the bag after it had been run at (+4,-15), removed from the baghouse, and opened up. Dust from the bottom and top of the bag was aspirated with a small tube and passed directly to a cascade impactor. Most samples were taken from the positive electrodes, which had the most evident accumulation of dust; a few samples were also taken from ground electrodes. Results are plotted in Figure 21 as log-probability curves. It can be seen that curves corresponding to the top and the bottom samples cluster separately, with mass mean diameters of about 3 μm and 10 μm, respectively. (The mean mass diameter can be read from the intersection of the curves in Figure 21 with the broken line at the 50% level.) Thus, the predicted segregation by size is detectable. Differences between dust collected on positive and ground wires are not resolved by these data.

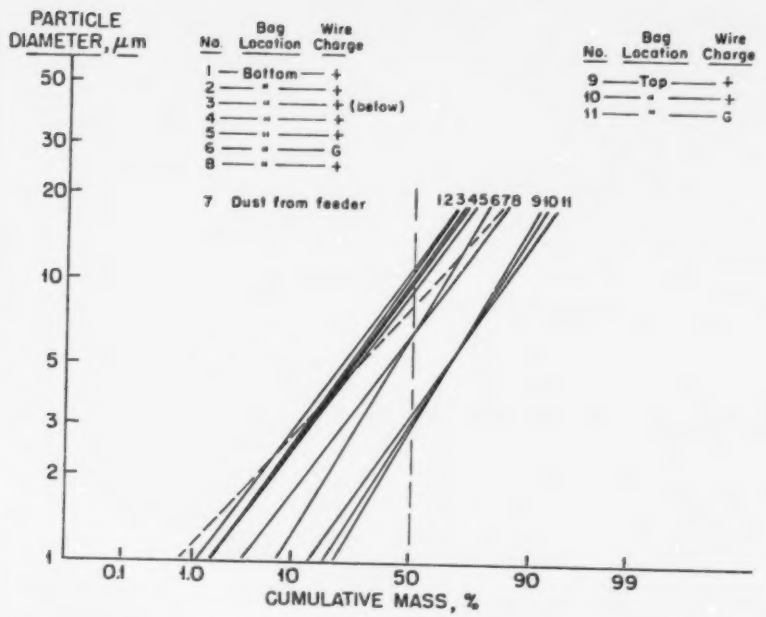

Figure 21. Cumulative distributions with respect to particle size for dust deposited at the top and bottom of a bag run at (+4,-15).

SECTION 5

PRINTED ELECTRODES

A different approach to the fixing of electrodes to filter fabrics is provided by what are being called "printed" electrodes (PE). The method of applying the electrode pattern to the fabric may not be strictly speaking a printing process, but the results have an appearance that strongly resembles print. The word may be used in the loose sense associated with "printed" circuits which are also not exactly printed but rather etched. The technique was developed by Wamsutta, a division of M. Lowenstein Corporation.

A sample of polyester felt with a pattern of parallel conducting stripes was obtained from Wamsutta, and initial measurements were made with patches of the material without conditioning the filter. The strong PDR-voltage relationship shown in Figure 22 was found.

A larger sample of the same polyester felt with similar conducting stripes was then obtained and sewn into a bag. The bag was mounted in the

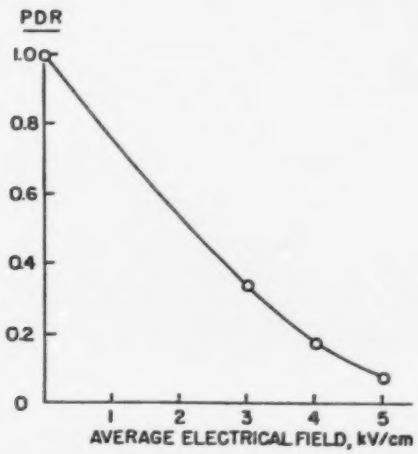

Figure 22. PDR-field relationship for new (unconditioned) polyester felt patch filter having printed electrodes.

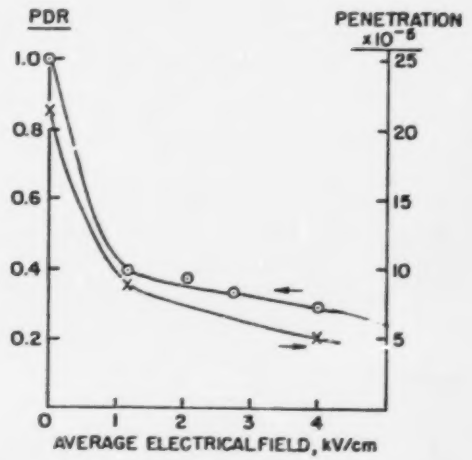

Figure 23. Performance of polyester felt bag fitted with printed electrodes and napped. PDR (o) and penetration (x).

baghouse and found to respond satisfactorily to electric stimulation as shown by the results in Figure 23. With the printed electrode bag, connection of the electrodes to the power supply was rapid and trouble-free, and no sparking problems were experienced at all. The advantages of this form of electrode are thus considerable, and efforts made to develop the technique further would be well spent.

The results in Table 4 were obtained at two face velocities: 3 and 1.5 cm/s (6 and 3 ft/min). Although the felt should operate satisfactorily at the higher velocity, it was found to develop a rather high pressure drop. At the lower velocity, the pressure drop remained at a more acceptable level.

TABLE 4. PRESSURE DROPS FOR POLYESTER FELT BAG WITH PRINTED ELECTRODES (Inlet concentration 7 g/m^3)

Field (kV/cm)	3 cm/s $\Delta p_i/\Delta p_f$ (mm H_2O)	PDR	1.5 cm/s $\Delta p_i/\Delta p_f$ (mm H_2O)	PDR
0	64/255		10/56	
1.14	60/234	0.91		
2	67/207	0.73	10/36	0.56
4	57/210	0.80	11/27	0.35

When similar measurements were attempted with PE applied to woven glass fabrics, very poor results were obtained. The problem was traced to the fact that woven fabrics have a greater in-plane shear compliance than felts, so that the PE break when the fabric is handled. Attempts were made to formulate a tougher PE material that would be flexible and also capable of resisting the temperature and chemical conditions found in baghouses. Materials tried included various epoxy compounds and Teflon® and polyvinylidene latexes, into which was mixed carbon black powder. It was found that a mass fraction of carbon black between 10 and 20 percent was sufficient to impart a suitable conductivity to the resin. However, when the resin hardened, whether by crosslinking or by solvent evaporation, the slight shrinkage placed the electrode under longitudinal tension. Even moderate handling of the fabric was then sufficient to destroy the conducting properties of the deposited stripe, and subsequent examination under the microscope showed many cracks.

For laboratory purposes, a composition of carbon black in a contact adhesive (Pliobond, Goodyear Tire and Rubber Co.) was found to have enough flexibility to resist considerable mechanical abuse without losing conductance. The results in Table 5 were obtained for patch filters having PE

with such a composition. They show that with woven glass fabrics as well as with felts, PE can yield pressure drop reductions as great as those with wire electrodes. It is almost certain, however, that at higher temperatures the adhesive would degrade, so that rubber-based PE would be suitable only for low temperature applications. The main purpose of this study was to demonstrate that PE could be effective in ESFF. The formulation of materials for a practical system is more appropriately left to a time of greater commercial interest in ESFF.

TABLE 5. COMPARISON OF PDR VALUES WITH PRINTED AND WIRE ELECTRODES
(Face velocity 2 cm/s; reverse air velocity 6 cm/s)

Field	J.P. Stevens 648/45		Spun glass	
(kV/cm)	Wires	Lowenstein PE	Wires	Rubber cement/ carbon black
2	0.91	0.82	0.83	0.87
4	0.76	0.72	0.60	0.52
6	0.67	0.64	0.31	0.27

SECTION 6

PROGRAMMED VOLTAGES

ESFF work in this laboratory up to this time has involved the use of constant DC voltages. It is by no means certain, however, that other voltage functions with respect to time could not give better results. To explore this possibility, a high voltage relay was obtained that allowed the filter electrodes to be connected to one or the other of two power supplies. Thus, if one power supply were set to a positive and the other to a negative voltage, the applied field at the filter could be changed in magnitude and direction by throwing a switch.

First measurements were made with polarity reversal during reverse air cleaning of the filter. Until then, the applied field had been kept at the same value throughout filtering and cleaning. Previous observations, however, supported the belief that cleaning might be aided by electrostatic means. On these occasions, brief application of a large voltage resulted in the shedding of accumulated dust, both at the macroscopic level, where dust was removed from a bag, and at the microscopic level, where particles were seen to fly off single fibers to which they were adhering. For the experiments reported here, the extent of cleaning was gauged from the magnitude of the initial pressure drop, Δp_i, in the cycle following cleaning. Values of Δp_i were measured after cleaning with and without electrostatic assistance and with filtering at various levels of applied field.

The effect of the duration of the reverse field applied during cleaning was examined first. It was found that 1.5 s and 15 s applications gave equivalent effects, so that it was assumed that time plays a minor role.

Results for the effects of the magnitude of the reverse voltage obtained with woven glass fabric are shown in Figure 24. There is clearly a significant effect on the initial pressure drop. However, the value of these results is diminished by two observations: The effectiveness of the voltage reversal is less when a voltage is applied during filtering, which is the likely condition seeing that the electrodes are present in the fabric for the sole purpose of providing electrostatic enhancement. Second, although significant reductions in the value of the residual pressure drop Δp_i are seen, the final pressure drop, after the dust cake has been built up again, is the same as when no voltage reversal is used to aid cleaning. This indicates that voltage reversal only clears a small space near the

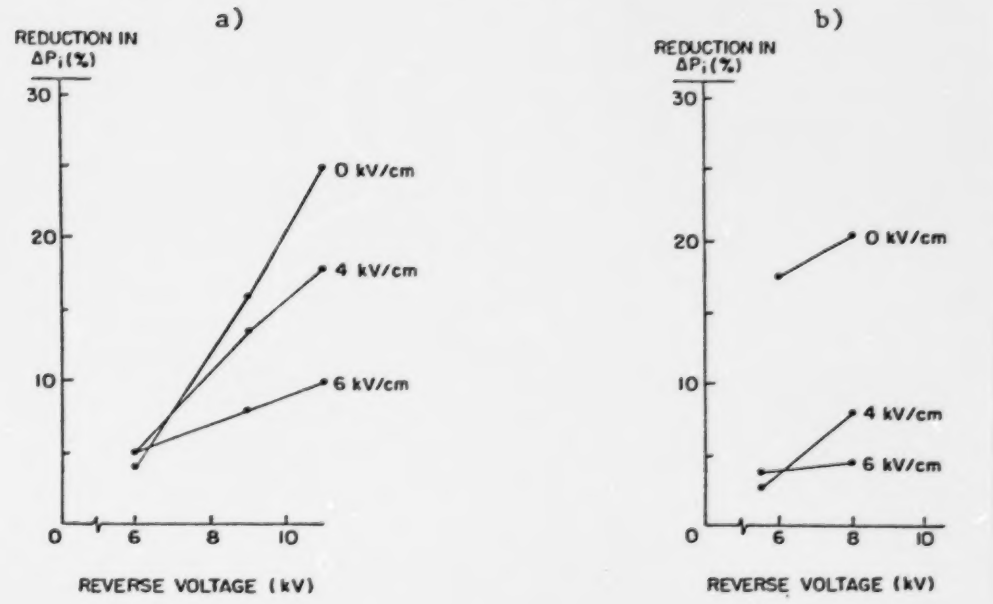

Figure 24. Effect of reverse polarity voltage during cleaning on initial pressure drop in following cycle.

a) Patch experiments using woven glass fabric at several filtering voltages.
b) Results for a bag made of the same woven glass fabric.

electrodes in which the dust cake quickly builds up again. A similar explanation accounts for the first observation; an applied voltage alone causes a lowering of the residual pressure drop which is therefore less affected by voltage reversal. Both these effects severely limit the value of electrostatic aid in cleaning by the method described.

A different insight into these events is derived from the data plotted in Figures 25 and 26. These were obtained by conditioning a woven glass filter patch for many cycles, and monitoring the pressure drop continuously and the mass of captured dust at intervals. The results confirm and simplify the previous observations. As the filter conditions, the mass of dust retained after cleaning (the "residual" dust) increases, and so does the

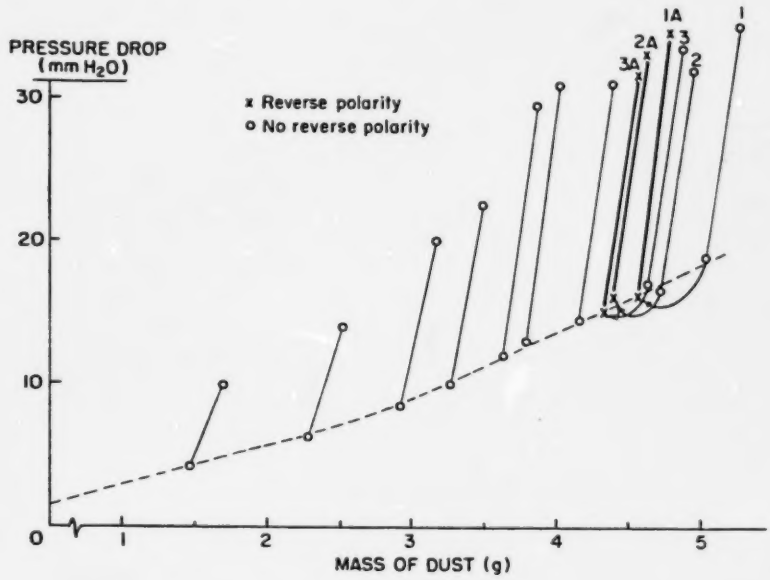

Figure 25. Initial (lower points) and final (upper points) pressure drops while conditioning a woven glass filter. The points marked x were obtained after reversal of ESFF voltage polarity during reverse air cleaning. The difference between "conditioning" (broken lines) and "filtering" cake resistance (full lines) is clearly seen. Constant field of 4 kV/cm; face velocity 6 cm/s.

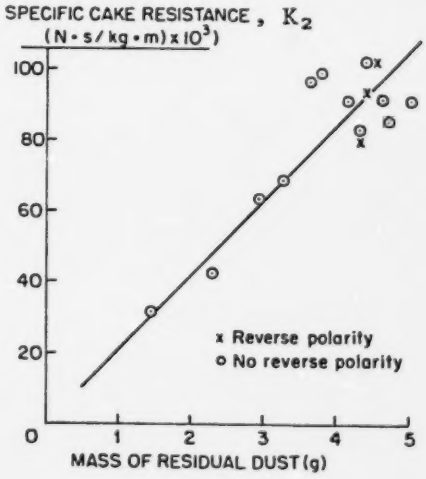

Figure 26. Dependence of "filtering" cake resistance (slope of final pressure drop curve, upper points in Figure 25) on mass of "conditioning" dust (mass at beginning of cycle, lower points in Figure 25).

residual pressure drop (lower points in Figure 25). The slope of the broken line may be taken as the specific cake resistance of "residual" dust; this is much lower than the slopes of the solid lines which are due to the dust deposited during filtering (the "filtered" dust). This difference is due to the location of the dust: residual dust is assumed to be deeper in the fabric. The specific cake resistance K_2 associated with the filtered dust also increases as the filter conditions (Figure 26). These observations are consistent with a model in which the residual dust is trapped in small pores, so that it has a small effect on permeability. Whether the two kinds of dust have different composition or particle size is not known, but it is reasonable to expect that residual dust contains smaller particles.

It appears that unless the structure of the dust deposits can be drastically changed, the only way to reduce pressure drop is by operating in a region closer to the origin in Figure 25, i.e., by reducing the amount of accumulated residual dust. It is clear that the reversal of polarity achieves only minor results in this direction if the reversal is applied to a filter that is already conditioned. In Figure 25 the points following polarity reversal are shown in heavier lines. Three pairs of cycles are shown. For example, after the conditions of cycle 1 were recorded, polarity reversal yielded cycle 1A. The same occurred with cycles 2 and 2A, and 3 and 3A. The resulting reduction in pressure drop is consistent with the other data points and amounts to only a few millimeters of water.

Further examination of programmed voltage for ESFF was made using AC voltages instead of DC for certain portions of the cycle. These measurements were made with a woven glass bag with stitched-in 150 μm diameter wire electrodes, using a face velocity of 3 cm/s and cleaning by reverse air. Several questions were addressed:

1. Comparison of PDR with AC and DC bag voltages
2. Same comparison with DC precharging
3. Same comparison with AC precharging
4. Comparison of efficiencies with AC or DC bag and precharger voltages
5. Relationship between voltage and current for AC

1. The PDR values obtained with AC voltages on the bag electrodes were plotted on a curve obtained previously with DC voltages (points marked x in Figure 27), and no significant differences were found. It must be noted, however, that with either DC or AC, the PDR values are rather high.

2. With a DC voltage on the precharger, PDR and penetration values were lower when the bag voltage was DC, as shown in Table 6.

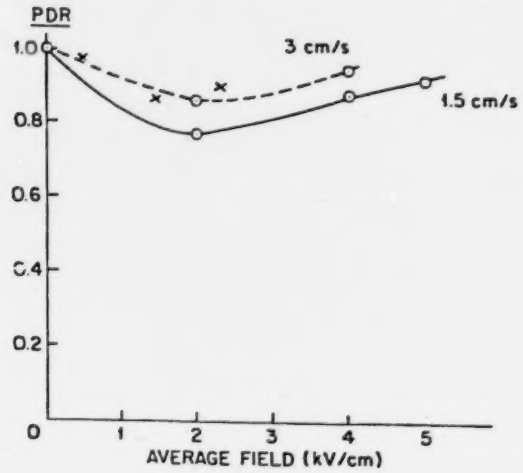

Figure 27. The effect of applied field on pressure drop.
o - DC voltage. x - AC voltage. 3 cm/s.

TABLE 6. PERFORMANCE WITH DC AND AC VOLTAGES ON BAG AND DC VOLTAGE ON PRECHARGER.

Bag voltage (kV)		Precharger voltage (kV DC)	PDR	Outlet concentration (g/m^3)
3.0	AC	-15	0.53	0.0236
4.75	AC	-15	0.35	0.0199
3.0	DC	-15	0.45	0.0180
4.75	DC	-15	0.26	0.0114

3. Comparison of DC and AC precharging was limited by the maximum AC voltage available at the time, namely 4.75 kV. The values in Table 7 were obtained. The resolution of the results is not strong, but the indications are that when DC is used instead of AC, either on the bag or on the precharger, lower PDR and lower outlet concentrations are obtained.

TABLE 7. PERFORMANCE WITH DC AND AC VOLTAGES ON BAG AND PRECHARGER

Bag voltage (kV)		Precharger voltage (kV)		PDR	Outlet concentration (g/m^3)
4.75	AC	4.75	DC	0.80	0.1136
4.75	DC	4.75	AC	0.83	0.0996
4.75	DC	4.75	DC	0.76	0.0944

4. Measurements of efficiency were made by sampling the air downstream of the bag. The results are reported in Tables 6 and 7 as outlet concentrations, which are proportional to dust penetration. It can be seen that in all cases a change from DC to AC voltage brings about an increase in outlet concentration. It may be assumed in the absence of any other explanation that, in some fraction of the AC cycle, the field is too weak to affect capture, and during this fraction penetration occurs at a higher level.

5. It was thought possible that the use of AC might be found to give an advantage in that higher voltages might be applied than with DC. The upper limit to the voltage that can be applied to a bag is determined by the current passed by the bag. It was found, however, that the currents exceeded those registered with the corresponding DC voltages (see Table 8). Thus using AC presents no clear advantage in allowing higher practicable bag voltage levels.

TABLE 8. CURRENT PASSED BY BAGS WITH APPLIED AC AND DC VOLTAGES

Bag voltage (kV)		Current (μA)
6	AC	175 to 200
7	AC	175 to 350
8	AC	300 to 600
8	DC	100 to 200

SECTION 7

CLEANING OF FABRIC FILTERS

BACKGROUND

A recent study has shown that, in order to enhance the economic advantage of fabric filtration over other methods of dust control, operations should be conducted at the greatest possible face velocity [9]. The area of filter cloth needed to process a certain flow of gas is inversely related to the face velocity, and a smaller cloth area would be accompanied by decreased hardware sizes and consequently lower capital costs. As a rule of thumb, costs vary inversely as face velocity.

An increase in face velocity, however, usually results in increased pressure drop and particle penetration, so that for a given set of conditions - fabric, dust composition and concentration, temperature - there is a velocity limit beyond which pressure drop and/or penetration becomes unacceptable. In seeking means to allow higher velocity operation, several approaches have already been taken. The potential of electrostatic aids for decreasing the penalty in Δp and penetration has been documented [9-11]. Studies of fabric structure have shown how performance may be improved by using fibers having modified geometry [12] and layered fabrics [11]. A third area of potential value is filter cleaning. This topic has received minor attention, yet it is relevant in this context, since the excessive pressure drop developed at higher velocities is usually the result of failure of the cleaning procedure to remove a mass of dust equal to that just collected. The retained dust mass thus increases gradually from cycle to cycle and leads to poor performance. There is a tendency for this to happen no matter how low the velocity, so that pressure drop increases as the filter becomes "conditioned". The concept of conditioning carries the implication that eventually a steady state is reached, but in reality, the pressure drop continues to increase approximately in proportion to log of time, and the rate of increase is greater at higher face velocities. Ideally, it should always be possible, no matter what the face velocity, to design a cleaning procedure that, by being sufficiently energetic and prolonged, would return the pressure drop to the same value. In practice it may be assumed that such vigorous cleaning is precluded by cost, by possible bag damage, and perhaps by a lack of information as to the best procedure to follow.

The success of a cleaning method in removing dust accumulation should also affect penetration. A woven fabric benefits from a certain amount of

dust cake buildup because the weave has many pinholes that at first allow leakage. When these pores are partially blocked with particles, there is a decrease in penetration. If, however, a dust cake is formed of sufficient thickness to cause a high pressure drop, local collapse of the cake may occur and penetration will again increase. With felts the effect of pinholes is minor, but with these materials seepage effects become more pronounced as the fabric becomes loaded with dust. Effective cleaning should thus be important in maintaining low penetration.

EXPERIMENTAL PROCEDURES

Three sets of measurements were made: the first with a Teflon® felt bag cleaned by pulse-jet, the second with a J. P. Stevens type 648 woven glass bag also cleaned by pulse-jet, and the third with a Teflon® felt bag cleaned by reverse air with shaking. All three bags were virtually unused, so that the trials began with a period of conditioning.

In all three cases, the procedure was to run the baghouse at different face velocities and measure pressure drop (Δp) and penetration at each velocity. The first run was at 3 cm/s (6 ft/min), and the air speed was increased in steps of 1.5 cm/s until either Δp or penetration moved out of an acceptable range. The speed was then reduced and increased again in the same steps to examine the ability of the bag to recover the better performance associated with lower speeds.

It was decided to do the pulse-jet cleaning off-line. To do this, the timers were connected so that (a) the main flow was interrupted just before the pulse, and (b) the pulse valve remained open for a few seconds after pulsing. The first measure was expected to allow dust blown off by the pulse to fall to the hopper before the next filtering cycle began. If the main flow is not interrupted, the dust is immediately redeposited on the bag a short distance below the point where it was dislodged. This redeposition, as might be expected, becomes more severe at higher face velocities, until eventually almost all the dust cake is redeposited, so that the pulse becomes ineffectual and pressure drops rise to large values. It was expected that the second measure might eliminate the "carpet beater" effect. It has been shown that penetration in pulse-jet bags is a maximum just after the pulse when the bag is driven back against the cage by the main flow. The impact appears to loosen the dust cake structure and promote seepage. Leith et al. [13] showed that this effect could be reduced by a secondary flow of air following the pulse which prevents the bag from rapidly collapsing onto the cage.

PULSE-JET RUNS

Results for the Teflon felt and woven glass bags with pulse-jet cleaning were so similar that they will be discussed together. The same conclusions apply to both.

Figures 28 and 29 show average Δp (i.e., $\frac{1}{2}[\Delta p_f + \Delta p_i]$) vs. face velocity; the values reached are reasonable in view of the rather high velocities.

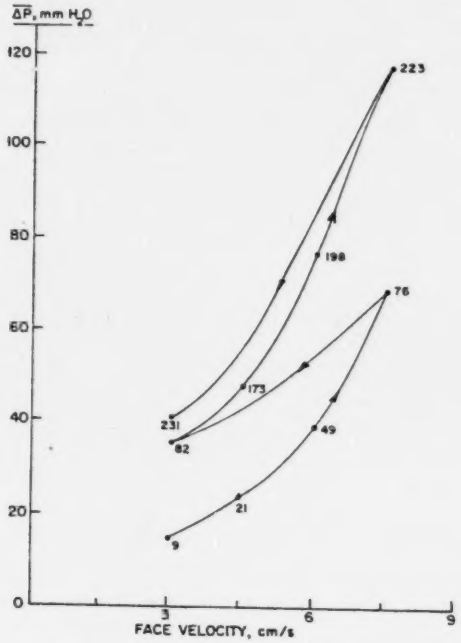

Figure 28. Dependence of average pressure drop on face velocity and running time (numbers near points indicate hours).
Teflon® bag cleaned by pulse-jet.

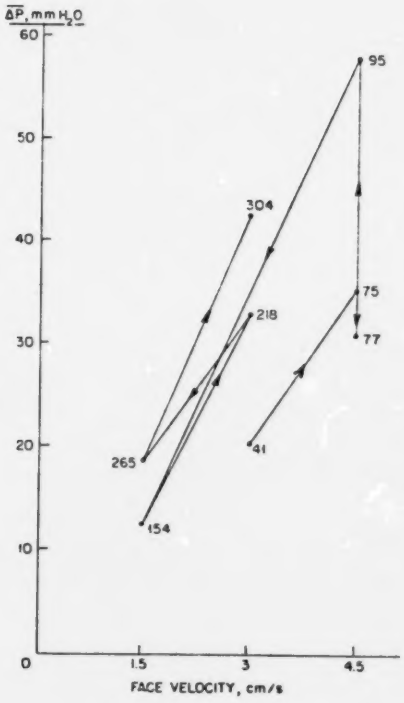

Figure 29. Dependence of average pressure drop on face velocity and running time.
Woven glass bag cleaned by pulse-jet.

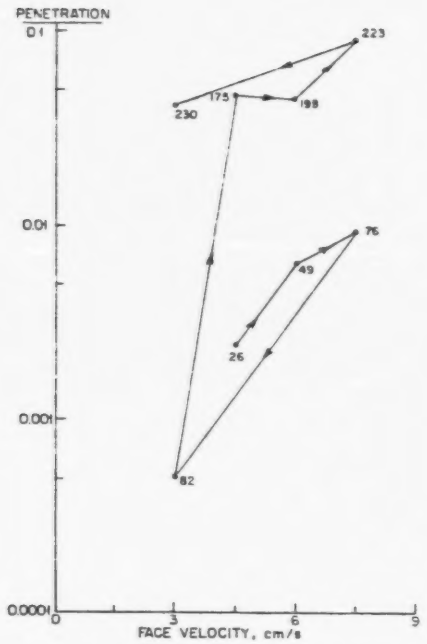

Figure 30. Dependence of penetration on face velocity and time for the conditions corresponding to Figure 28.

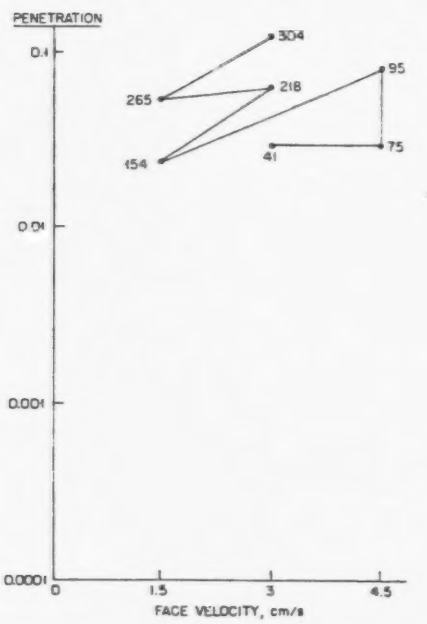

Figure 31. Dependence of penetration on face velocity and time for the conditions corresponding to Figure 29.

Face velocities were varied up and down between 3 and 7.5 cm/s, and the figures show that there is a certain time effect, but that after ∿200 hours the "hysteresis" loops have narrowed, indicating that some kind of steady state has been approached.

On the other hand, inspection of the penetration curves (Figures 30 and 31) reveals an unexpected situation, because as time progresses, penetration levels continue to increase with time, and by the time the runs were stopped, had reached the region of 5 to 10%. Reducing the face velocity to the regular operating range of 3 cm/s did not always bring about a reduction in penetration, which means that the accumulated dust causes a permanent change in the penetration mechanism. This could conceivably involve interfiber spaces being "wedged" open by dust aggregates, or some other unknown reason for the breakdown in the process whereby dust is normally captured. This phenomenon is worth studying more closely because it appears to provide evidence of a penetration mechanism different from the "carpet beater" effect described by Leith et al. [13].

REVERSE AIR RUNS WITH SHAKING

Measurements of Δp and penetration were made with the Teflon bag in the same type of sequence used with the pulse-jet runs. Face velocities were increased in 1.5 cm/s steps beginning at 3 cm/s, and reverse air velocities were made equal to the forward velocities.

Qualitatively, the results are roughly opposite to those obtained with pulse-jet, where penetration increased to high levels with time and increasing face velocity, but Δp levels reached quasi-steady states. In contrast, with shaker-reverse air, penetration remained below 1%, as can be seen in Figures 32 and 33, but pressure drops rose to high levels and did not approach steady states. Figure 34 shows how even with electrical stimulation (ESFF) and precharging the dust (+4,-15), Δp reached 400 mm of water at 5.5 cm/s face velocity. The drop in Δp between 260 and 288 hours was the result of adjustment of the shaker mechanism.

In conclusion, there was a large difference in the performance of the same fabric depending on whether it was cleaned by pulse-jet or by shaking with reverse air. There is a large difference in the energy input for the two methods. With the shaker used in our baghouse, the energy release per shake was 0.4 J or about 1 J/m^2 of fabric. Since cleaning involved 8 shakes, the total energy was of the order of 10 J/m^2. This may be contrasted with the energy of a 30 psi pulse, which was calculated to be 350 J/m^2 for the dimensions of our pulse-jet unit.

These results are in general agreement with those of Dennis and Wilder [14], who report that penetration for pulse-jet cleaned bags is 10 to 100 times higher than for mechanically shaken reverse air systems. They also found that penetration increased with the pulse energy. It appears, therefore, that cleaning methods that use some form of mechanical impact permit only a trade-off between excessive pressure drop or excessive penetration, depending on whether the impact energy is low or high.

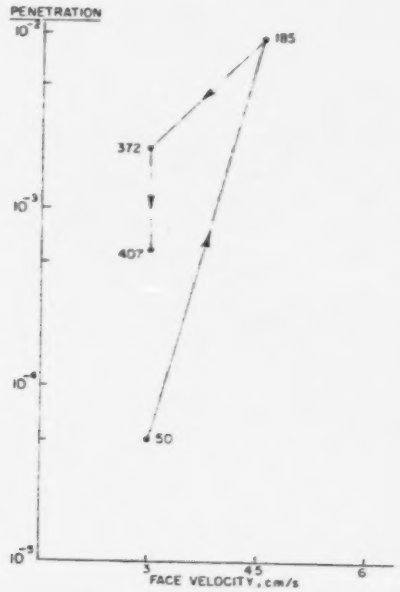

Figure 32. Dependence of penetration on face velocity and running time. Teflon® bag cleaned by reverse air.

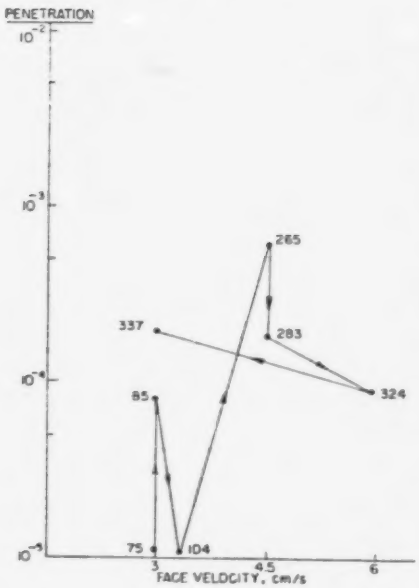

Figure 33. As Figure 32, but with 4 kV/cm average field on bag, -15 kV on precharger (+4,-15).

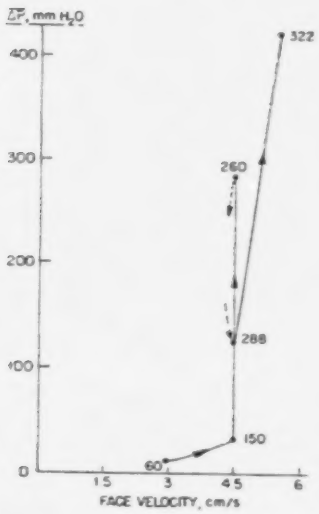

Figure 34. Dependence of average pressure drop on face velocity and running time for the conditions corresponding to Figure 33 (+4,-15).

It would seem profitable then to inquire whether cleaning methods based on different principles might offer more rewarding alternatives.

CLEANING BY BAG SHEARING

The data in Figure 25 illustrate what is intuitively reasonable, namely that residual pressure drop is due to dust lodged within the structure of the fabric, while the rise in pressure drop during filtration is due to more superficial dust. To dislodge the residual dust without shaking, a technique was explored which involved shearing of the bag fabric. In addition to being potentially harmful to the bag, shaking has the drawback of not cleaning every portion of the bag since nodes may occur where the shaking intensity is a minimum. If a baghouse is operating with ESFF, it may be a further disadvantage that contact between neighboring bags and consequent short circuiting may occur. The function of shaking is to provide a mechanical supplement to the cleaning action of the reverse air flow. There is thus no reason why mechanical modes other than shaking should not be equally effective.

One such mode consists of applying a shear strain to the bag. Since the bag is a cylinder, this can be done simply by turning the top support about the bag axis. The advantage of this procedure is that it is potentially less traumatic and theoretically affects every element of the bag equally. When a fabric is sheared, especially a woven fabric, each elemental space bounded by two neighboring warp and fill yarns will be transformed from a rectangle to a parallelogram. If the space were filled with dust accumulation, the shearing strain would tend to crush the dust aggregate and allow it to be more easily removed by the reverse air flow.

To twist the top bag support, it was encircled with strings which passed through a small hole in the baghouse wall and could be manipulated from the outside. The distance through which the strings had to be pulled to give a certain twist angle was determined beforehand. The shaker was disconnected.

The results of tests performed at different twist angles and numbers of twists are shown in Table 9. These measurements were made after only three cycles and are therefore far from representing steady state conditions. The values in the table refer to the effects of twist cleaning on residual and final pressure drops. Each twist consisted of turning the bag support through the listed angle, first clockwise, then counterclockwise to a negative value of the same angle, and back to the starting point. This was repeated for measurements marked two twists. The results show that "twice" was significantly more effective than "once", and that a larger twist angle reduces pressure drop more than a smaller one.

Further results, obtained after ten cycles at each condition, are given in Table 10. Here a comparison is made with shaker cleaning, and it can be seen that mechanical agitation, whether twisting or shaking, is an important component of the cleaning procedure. It can also be seen that twisting is as effective as shaking.

TABLE 9. RATIO OF PRESSURE DROP AFTER TWISTING TO THAT WITHOUT TWISTING AT SEVERAL TWIST ANGLES AND NUMBERS OF TWISTS

Twist angle	One twist		Two twists	
	Δp_i (mm H_2O)	Δp_f (mm H_2O)	Δp_i (mm H_2O)	Δp_f (mm H_2O)
2.1°	0.81	0.97	0.60	0.85
4.1°	0.80	0.97	0.64	0.84
6.2°	0.55	0.91	0.44	0.81

TABLE 10. COMPARISON OF PRESSURE DROPS AFTER SHEAR AND SHAKER CLEANING

Cleaning method	Δp_i (mm H_2O)	Δp_f (mm H_2O)	$\Delta p = \Delta p_f - \Delta p_i$ (mm H_2O)
Twist, 2x, 2.1°	10.6	38.1	27.5
Twist, 2x, 4.1°	8.5	35.1	26.6
Twist, 2x, 6.2°	7.3	32.8	25.5
Shake	7.8	32.9	25.1
No shake, no twist	12.2	41.7	29.5

SECTION 8

PRESSURE DROP REDUCTION BY UPSTREAM DISPLACEMENT OF DUST CAKE

INTRODUCTION

If there is no large-scale displacement of dust over the surface of a filter bag, as might be the case with low levels of charge, the important mechanism then becomes the displacement of dust deposition in the upstream direction, that is, from the interior of the fabric toward the surface facing the oncoming aerosol. In a typical fabric filter, there are fewer fibers per unit volume at the surface of the fabric than in the interior. It has been proposed [15] that when no electric field is present, the dust penetrates the low density surface region and deposits below the surface where the fibers are closer together, and plugging of the interstices leads to high pressure drops. When an electric field is applied, the capture efficiency of the fibers is increased by an order of magnitude or more [16], so that the dust now deposits in the surface region. Thus the dust distribution is effectively shifted upstream where the fibers are further apart and can accommodate more dust before plugging occurs.

Evidence for this mechanism rests on visual observations of the surface of fabric filters and a series of experiments by Lamb and Costanza [15]. They used filters composed of two layers and found that lowering the fiber volume fraction of the upstream layer enhances the effect of the electric field in reducing the pressure drop.

EXPERIMENTS WITH TWO-LAYER FILTERS

A series of experiments were performed to determine the depthwise dust distribution in a fabric filter as a function of the mass of dust deposited per unit area, M, the face velocity of the aerosol, U, and the applied electric field, E. The experiments involved depositing fly ash onto multilayered filters (usually two or three layers) and weighing each layer before and after deposition. The layers in the filter were made so as to emphasize the effect of a low density surface layer; the upstream layer had a fiber volume fraction of 0.02 compared with 0.23 for the downstream layer. A "patch" filtration apparatus was used (Figure 35) rather than a filter bag. It should also be noted that in all the studies presented here the results are for "first cycle" dust; the effects of filter cleaning or conditioning were not addressed.

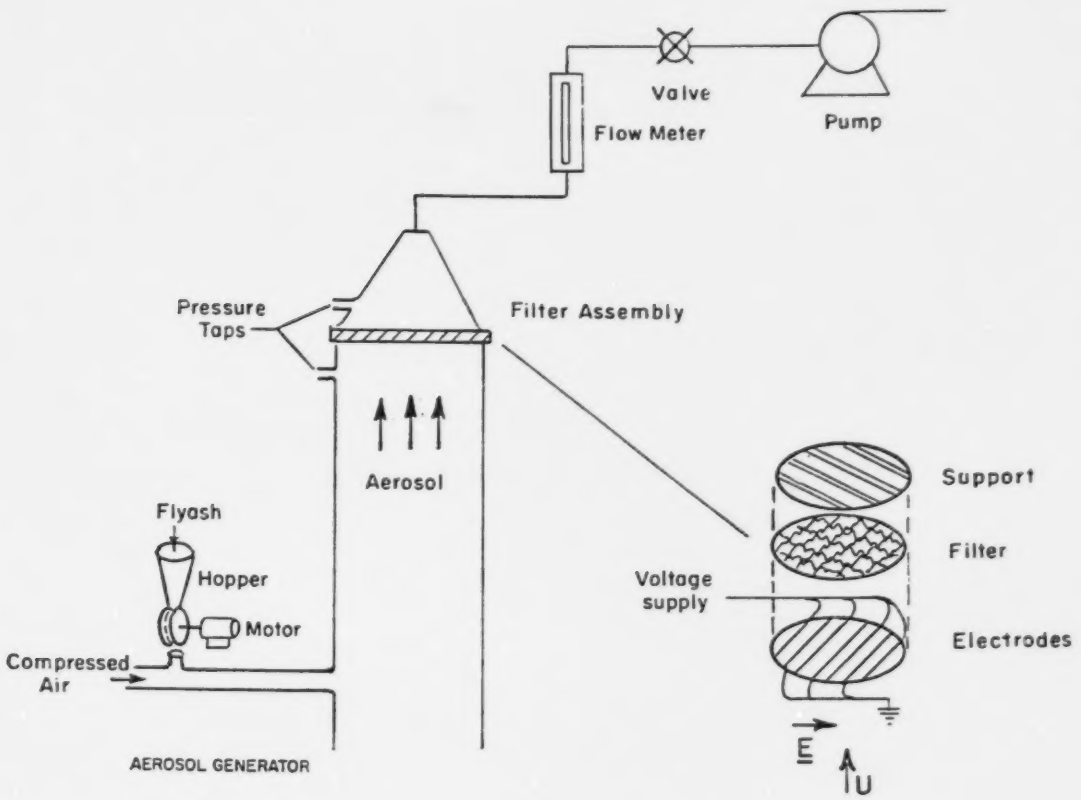

Figure 35. Schematic of filter apparatus.

The "fluffy" upstream layers of the filters were made by compressing a carded mat of 3 den (17 μm) 1.5 inch crimped PET (polyethylene terephthalate) fibers to a thickness of 1.6 mm in a hot press. A small fraction of vinyon, a low softening point bonding fiber, was added to the PET during the carding process and when pressed under heat, fused to the PET fibers to give the final filter layer structural integrity. It is difficult to measure the volume fraction of fibers accurately in such low density mats, because of the difficulty in measuring their thickness accurately. Nevertheless, the solidity (volume fraction of fibers, or one minus porosity) was calculated for all specimens from the compressed thickness (1.6 mm), and was found to range between 0.015 and 0.02. The downstream layer was a needlepunched PET fabric with a thickness of 1.7 mm and a solidity of 0.23. The fibers were 20 μm in diameter. In some experiments a third layer, identical to the upstream layer, was added, so that

the filter consisted of two low solidity upstream layers followed by the high solidity downstream layer.

RESULTS AND DISCUSSION

Figure 36 shows the fraction of dust deposited in the upstream layer as a function of the applied potential for three-layer filters. Three things can be observed in this figure. First, it shows quite clearly that as the potential is increased from 0 to 3 kV, the fraction of dust in the upstream region is increased substantially. Secondly, a greater fraction of the dust deposits in the upstream layer when the face velocity is increased from 3 to 6 cm/s; this reflects the increase in efficiency due to impaction at higher velocity which occurs for particles greater than 1 μm in diameter (Appendix 8A shows that more than 90% of the fly ash used is in the size range greater than 1 μm).

Finally, particularly in the absence of a field (0 kV), there is a good deal of scatter in the data, chiefly because the measurements were made at different dust loadings. In Figure 37 the fraction of dust in the upstream layer is plotted against the total dust loading, M, for the no-field data. It can be seen that as M increases from 0 to 20 mg/cm^2, there is an almost linear increase in the fraction of dust in the upstream layer. (The fraction of dust in the middle layer, which has the same low solidity as the upstream layer, remains essentially constant.) The reason is that as more dust accumulates on the fibers, a greater projected area is exposed to the flow, so that the fibers become more efficient in capturing particles. Much of the scatter in Figure 36 can be removed by plotting results obtained at a single dust loading. This is done in Figure 38a, which gives the dust fraction in the upstream layer of a two-layer filter as a function of applied potential at a dust loading of 11.9 mg/cm^2. The fraction of dust in the upstream layer increases from 40% at 0 kV to 85% at 6 kV. Thus, the applied electric field does indeed shift the dust distribution upstream to regions of low solidity. Figure 38b shows the corresponding reduction in pressure drop as a function of applied potential.

CROSS-SECTIONAL VIEWS

Along with the dust distribution within the fabric, the structure of the dust cake may also contribute to the reduction of pressure drop by an electric field. Previous observations of the cake structure have been limited to "top views" of the fabric [15,17]. With no field present, the dust cake is continuous, plugging pores in the high density interior region (Figure 39b). When an electric field is applied, the dust tends to accumulate around invididual fibers at the upstream surface (Figure 39c). While these observations are significant, they do not directly show how the cake structure varies with depth into the filter. For this purpose cross-sectional views are needed, but in the past these have been impossible to obtain because of the fragility of the dust cake. Felix and Smith [18] developed a technique to embed a dust-loaded filter with a low viscosity epoxy, but they were dealing with strongly bound residual dust. The loosely

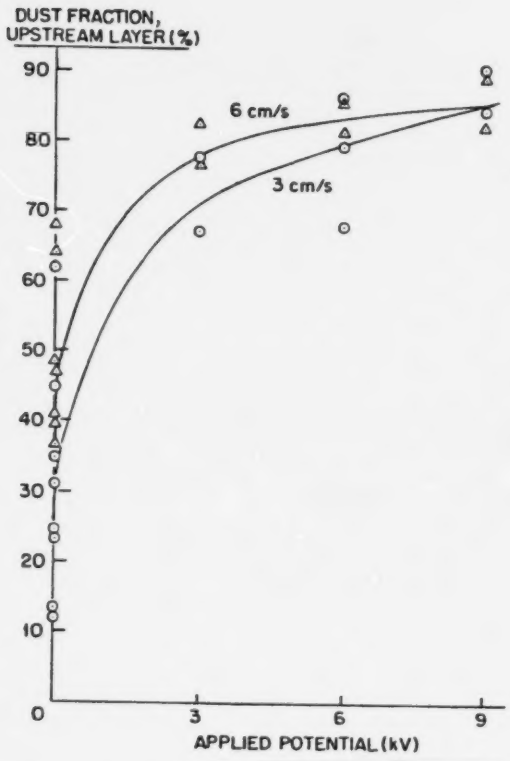

Figure 36. Effect of applied potential on dust distribution in a 3-layer filter.

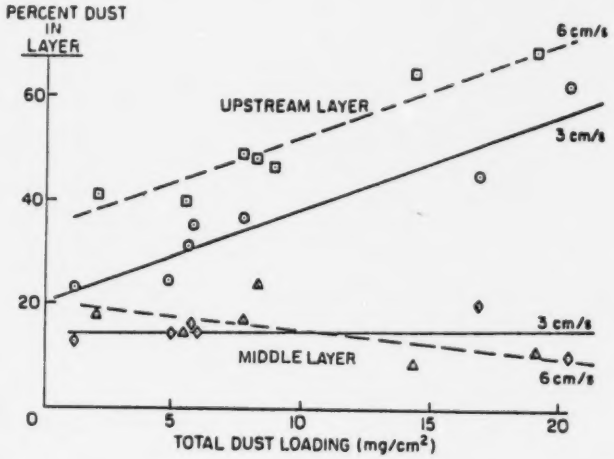

Figure 37. Effect of dust loading on its distribution in a 3-layer filter with no applied potential.

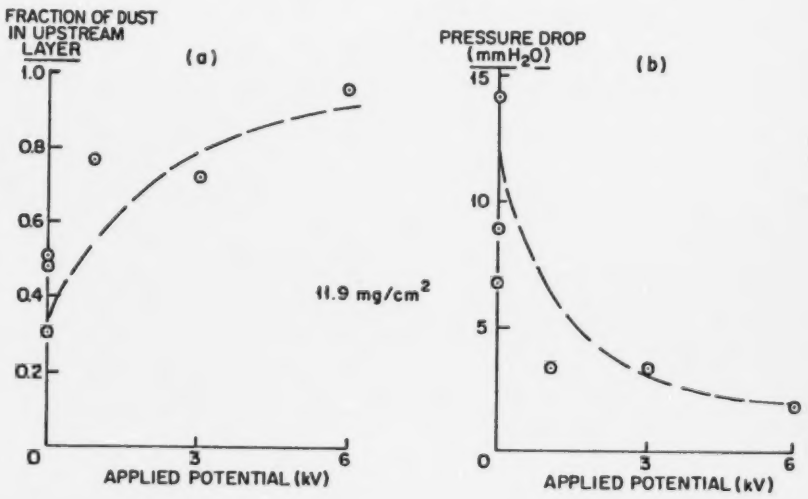

Figure 38. a) Dust distribution in a 2-layer filter as a function of applied potential for one dust loading (11.9 mg/cm^2) & velocity (3 cm/s).
b) Corresponding pressure drop as a function of applied potential.

Reproduced from
best available copy.

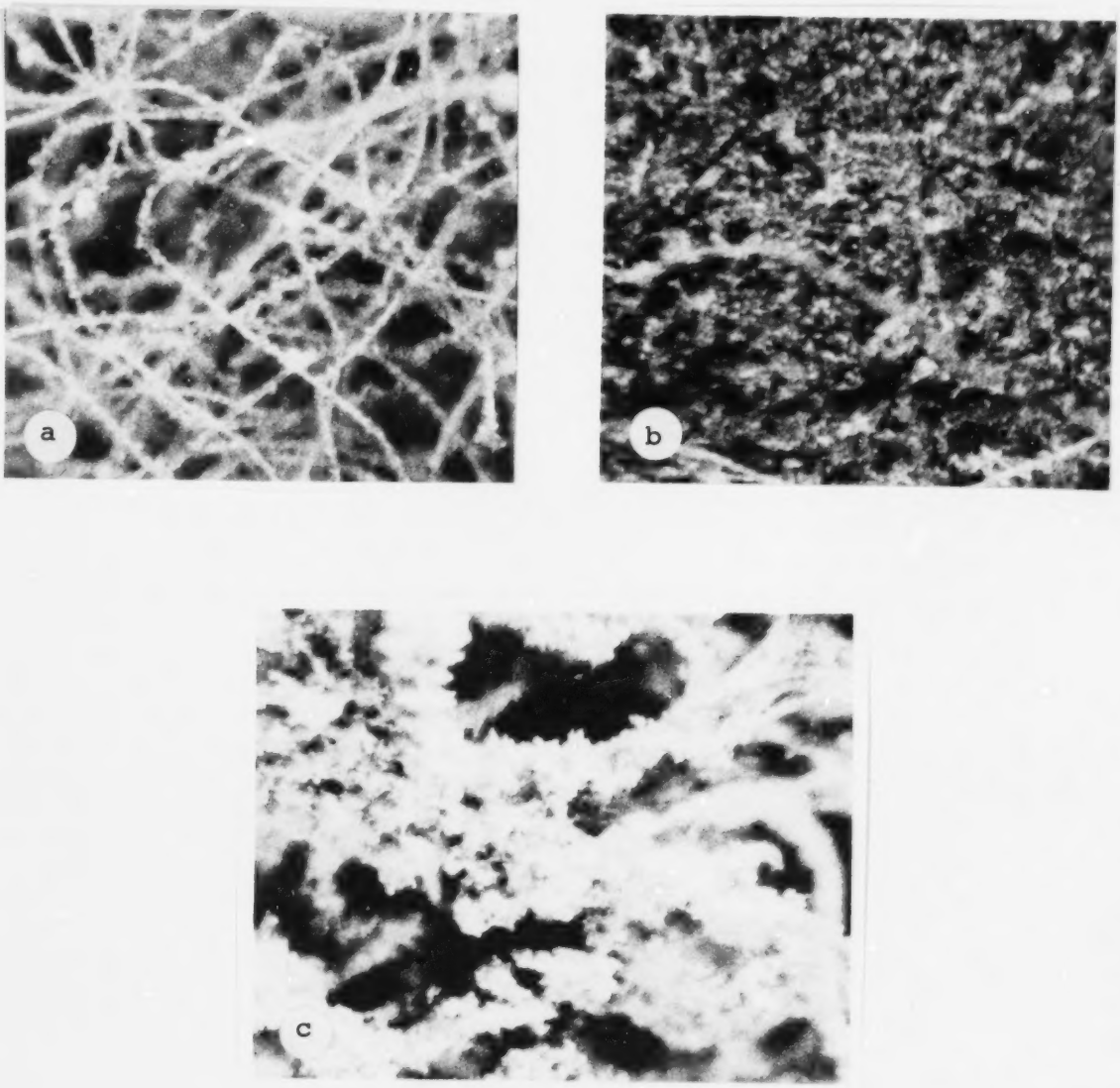

Figure 39. Top views of dust cakes.

a) No electric field, upstream layer.
b) No electric field, downstream layer.
c) 4 kV/cm, upstream layer.
(Very little dust collects on the downstream layer.)

bound "first cycle" dust on our filters is much more fragile and cannot withstand the viscous and surface tension forces of the embedding medium. Attempts to embed these filters with an epoxy were not successful.

A new technique was therefore developed, which eliminates this problem by first fixing the particles in place with the vapor of cyanoacrylate, the active ingredient of some instant adhesives. The fixing procedure is shown schematically in Figure 40. Cyanoacrylate vapor is passed over the sample and as it condenses, it polymerizes, forming a thin, clear film around the particles and fibers. The film bonds the particles in place but does not seem to disturb the cake structure in any way. Once the fixation process is complete, the filter can be handled without altering the dust cake.

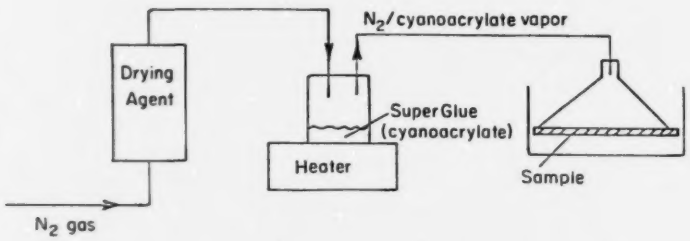

Figure 40. Schematic of fixation process.

Cyanoacrylate polymerizes in the presence of water, and so it is important that the sample be moist and the vapor dry until it contacts the sample. Dry nitrogen is used to carry the cyanoacrylate vapor to the sample. Usually the natural moisture of the sample on a humid day (>60% RH) is sufficient to catalyze the polymerization. Additional moisture can be provided by putting a source of steam under the sample as the glue vapor is fed through it. The nitrogen-cyanoacrylate bonding process takes about an hour at flow rates low enough to keep the dust cake intact. After being fixed, the sample is embedded in a clear medium for sectioning. Spurr's low viscosity embedding medium was found to work well for this application. The ingredients in this material are given in Table 11.

The samples are placed in gelatin capsules, potted, and cured by heating at 70°C overnight. The gelatin is later removed by immersion in water. Cured samples are then prepared for inspection under a microscope by slicing with a microtome. An ordinary light microscope is sufficient for studying the microscopic properties of the cake structure. Figure 41 shows an example of the structure revealed by this procedure.

TABLE 11. COMPONENTS OF SPURR'S LOW VISCOSITY EMBEDDING MEDIUM

4-Vinylcyclohexene dioxide (ERL-4206 or UNOX Epoxide 206)	10.0 g
Hardener NSA (nonenyl succinic anhydride)	26.0 g
Plasticizer DER 736 (diglycidyl ether of polypropylene glycol)	6.0 g
Accelerator S-1 (DMAE: Dimethyl-aminoethanol)	0.4 g

Figure 41a is the control case where no electric field has been applied. The filter is composed of a top layer with solidity 0.015-0.02 and thickness 1.6 mm, and a bottom layer with solidity 0.23 and thickness 1.7 mm. The fibers in both layers are approximately 20 μm in diameter. Aerosol flow was from top to bottom in the picture, and the dark areas represent fly ash deposit. For this particular run, 13.8 mg/cm^2 of dust were collected, and the increase in pressure drop due to the dust was 12.8 mm H_2O. The aerosol face velocity was 3.7 cm/s.

Figure 41b shows a similar filter under the same conditions except that an electric field of nominal strength 4 kV/cm was applied. Here, 17.3 mg/cm^2 of dust were deposited, but the increase in pressure drop was only 0.4 mm H_2O.

These photographs show the strong difference in dust placement due to the electric field. Without a field almost all the dust penetrates the low density upstream layer and deposits, in an almost continuous structure, at the dense layer interface. The pores are plugged. When the field is present, very little dust penetrates the upstream layer, and dust deposits around individual fibers, creating a very porous structure.

Qualitatively, the appearance of the dust structure remains like that in Figure 41b when the electric field strength varies from 0.67 kV/cm to 4 kV/cm, or when the face velocity doubles to 7.2 cm/s. Precharging the particles (no electric field) also yields a structure similar to that in Figure 41b, with more dust at the surface deposited around individual fibers than at the interface between layers, as does applying an electric field in addition to precharging the particles.

PRESSURE DROP DISTRIBUTION

To determine if the shift in dust distribution upstream to regions of lower fiber volume fraction is enough to account for the observed pressure drop reduction, the pressure drop across the individual layers of the

multilayered filters was measured as dust accumulated. In one set of experiments, a single layer was studied. In a second set, a complete multilayered filter was placed in the apparatus and pressure taps made of 1.3 mm diameter Teflon® tubing were inserted between the layers. The taps were positioned so that the ends were flush with the wall of the flow chamber, ensuring that a static pressure was measured.

Figure 42 shows a typical pressure drop vs. time curve for the low density upstream layer. The shape of the curve is the same as found by other investigators, viz., an exponential rise followed by a linear increase. The exponential rise is attributed to the filling of the pores and the linear region to the steady buildup of a uniform dust cake. The slope of the linear region was the same for both 0 kV and 1 kV potentials. At 6 kV, the linear region was never obtained, and the time constant of the exponential region was extremely small.

Figure 43 shows pressure drop as a function of dust accumulated in single layers placed in the apparatus with no electric field. The low fiber volume fraction filter ($c = 0.018$) has a much greater "capacity" for dust at a given pressure drop than the high solidity filter ($c = 0.23$), as expected. This indicates that shifting dust upstream to regions of lower solidity can by itself account for large reductions in pressure drop.

The effect of the electric field on pressure drop above and beyond this simple shift in dust distribution was examined by measuring the pressure drop across the individual layers of a two-layer filter using the technique described above. The results are shown in Figures 44 and 45 for the two different layers. The dashed lines represent the data from the single layer, 0 kV experiments for reference. The small disagreement between the single and two-layer results is probably due to compression of the probes at the wall.

Experiments were run at potentials of 0, 1, and 6 kV. Above 1 kV an interesting phenomenon occurred; no dust collected in a narrow ($\sim$2 mm) band just below the electrodes. This void region was present at both sets of electrodes but was more distinct on the high potential ones. It was also observed that most of the dust that penetrated the surface layer often deposited directly below the electrodes, suggesting that some of the dust repelled by the electrodes was actually forced deeper into the fabric. The evidence for this conclusion is not complete, and the phenomenon merits further study. This surface redistribution of the dust is exactly opposite to the phenomenon reported in an earlier section for the tubular bag geometry, where preferential deposition occurred on the electrodes when an electric field was applied. The reason for the difference in behavior for the two geometries is unknown but is thought to be associated with corona charging.

The results for the low solidity upstream layer are shown in Figure 44. With an applied potential, more dust is collected at a given pressure drop than in the 0 kV control case. Since the slopes of the linear region of the Δp vs. time curves are the same, this suggests that the

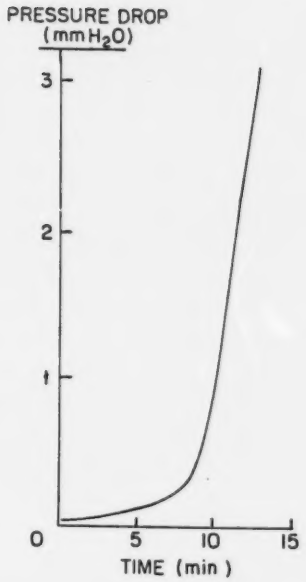

Figure 42. Pressure drop vs. time for a low solidity (c = 0.017) filter layer at low potentials (≲1 kV).

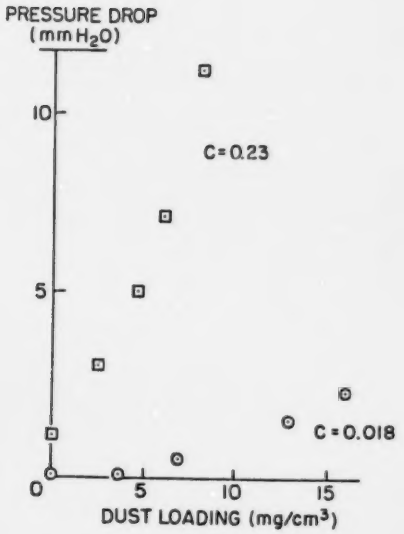

Figure 43. Pressure drop vs. dust loading and filter solidity, c. 0 kV.

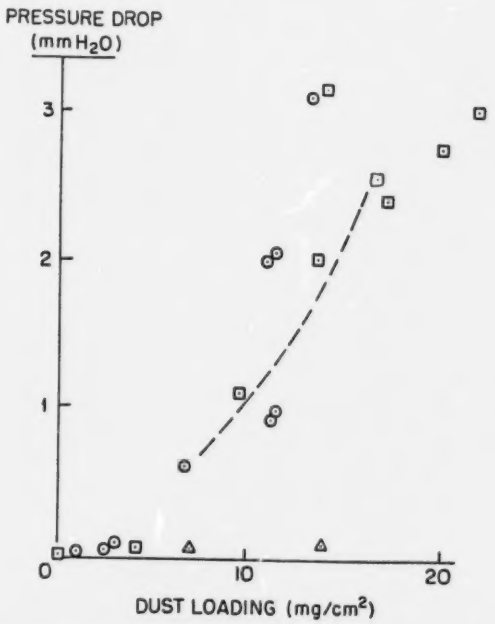

Figure 44. Pressure drop across upstream layer (c = 0.017) of a 2-layer filter. o-0 kV, □-1 kV, △-6 kV. Dashed curve - single layer, 0 kV data.

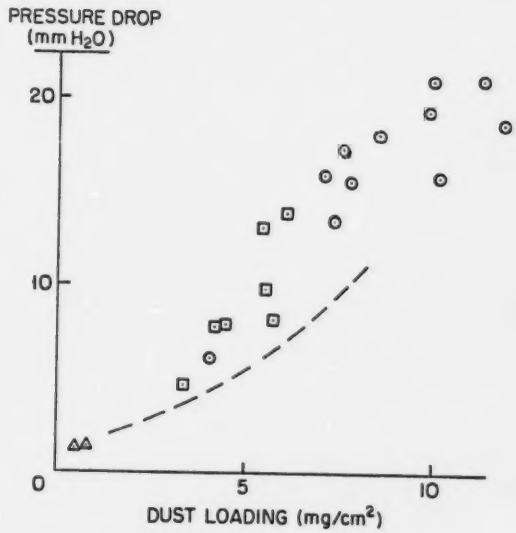

Figure 45. Pressure drop across downstream layer (c = 0.23) of a 2-layer filter. Symbols as in Figure 44.

electric field delays the onset of plugging, in support of the observation of the dust cake structure in the cross-sectional views.

For the high solidity downstream layer (Figure 45) any effect of the electric field is weak. The 0 kV and 1 kV data are essentially linear with M, suggesting that even at these small dust loadings the interstices are plugged and a uniform dust cake is developed. The onset of plugging does not seem to be affected by the electric field. Perhaps this is because the pore sizes are small to begin with, and the fibers, being further from the origin of the electric field, do not feel the full effect of the electrical forces. Since the efficiency of the upstream layer is so greatly enhanced by the electric field, data for the high potentials is limited to very small dust loadings, so that no trends can be deduced.

APPENDIX 8A

TABLE 8A1. PARTICLE SIZE DISTRIBUTION FOR A SAMPLE OF MERCER COUNTY, NEW JERSEY, FLY ASH (IMPACTOR ANALYSIS)

Aerodynamic size range (μm)	Most likely diameter (μm)	Mass (mg)	Mass fraction	Number fraction
50-17.2	33.6	148	0.292	0.051
17.2-9.7	13.45	128	0.2525	0.000689
9.7-5.7	7.7	89	0.1755	0.00255
5.7-3.4	4.55	65	0.1282	0.00903
3.4-1.9	2.65	46	0.0907	0.0324
1.9-1.05	1.475	24	0.0473	0.0979
1.05-0.5	0.775	4	0.00789	0.1125
0.5-0.25	0.375	3	0.00592	0.7449

$$D_{vs} = \frac{\Sigma n_i D_i^3}{\Sigma n_i D_i^2} = (\Sigma w_i / D_i)^{-1} = 5.86 \ \mu m$$

$$D_{v\ell} = \left[\frac{\Sigma n_i D_i^3}{\Sigma n_i D_i}\right]^{\frac{1}{2}} = [\Sigma w_i / D_i]^{-\frac{1}{2}} = 3.15 \ \mu m$$

SECTION 9

MODELING OF PRESSURE DROP ACROSS DUST LADEN FILTERS

INTRODUCTION

The results of the preceding section were complemented by calculations of the pressure drop across fibrous mats both clean and loaded with dust accumulations in different configurations, with particular attention to dust configurations obtained with electric fields. The approach taken was first to choose an appropriate model for the pressure drop Δp across a clean filter of uniform fiber volume fraction:

$$\frac{\Delta p a^2}{\mu U h} = f(c)$$

where a = fiber radius, μ = air viscosity, U = face velocity, h = depth of filter, and c = fiber volume fraction. This model was then modifed to include dust loading by increasing c (decreasing the overall porosity of the filter to reflect the addition of solids) and using an effective fiber radius to incorporate the microstructure of the dust cake. Finally, a model filter was devised to represent the distribution of c within the filter used in the experiments to see how the macroscopic shift in dust distribution affects the drag.

CLEAN FILTER

At low Reynolds numbers, the pressure drop across a clean fiber mat has the general form

$$\frac{\Delta p a^2}{\mu U h} = \frac{Ac}{-\ln c + f(c)} \quad , \qquad (1)$$

where A is a constant. A series of pressure drop measurements were made on a column carefully packed with mats of carded fibers. The variables included U, a, and c. One of the models which fits the data, shown in Figure 46, is the Happel cell model [19]. Although several of the assumptions made in this model are obviously wrong (for example, all the fibers are assumed to be parallel to the flow), it has the correct form:

$$\frac{\Delta p a^2}{\mu U h} = \frac{4c}{-\ln c + 2c - \frac{c^2}{2} - \frac{3}{2}} \quad . \qquad (2)$$

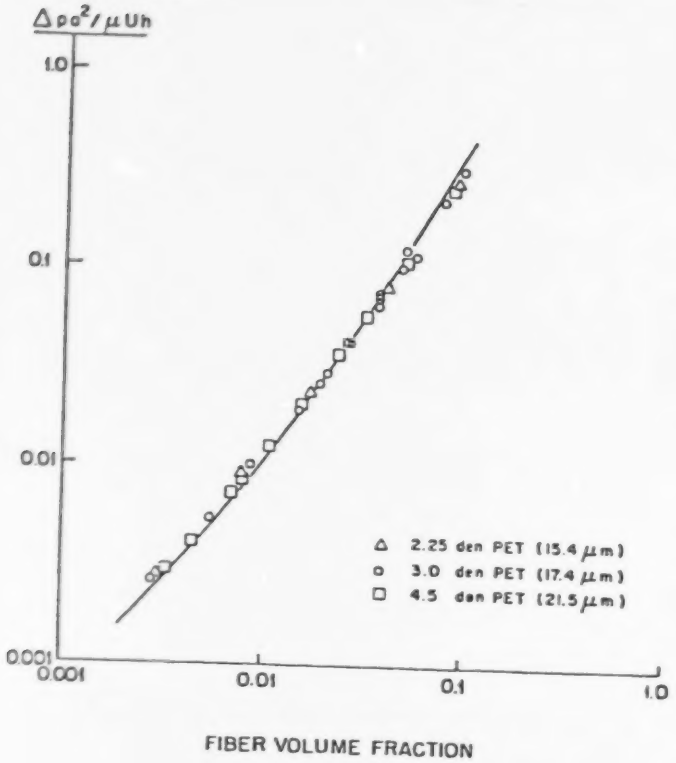

Figure 46. Results of measurements on a column packed with PET fibers. The curve is calculated using the Happel cell model for fibers parallel to the flow.

Since it provides such a good empirical fit for the packed column data, it was used as the basis for the dust laden model.

DUST LOADING

Many investigators [20] have assumed that a distinct dust cake forms as dust is deposited, so that the increase in pressure drop due to the dust is independent of the fibers:

$$\Delta p = \Delta p_1 + K_2 \, MU \quad . \tag{3}$$

Here, Δp_1 = pressure drop across clean filter

U = face velocity

M = dust loading, mass per unit area

K_2 = specific cake resistance = $\frac{\Delta p - \Delta p_1}{MU} = \frac{1}{k} \frac{\mu}{\rho_p (1-\varepsilon)}$

where k = permeability of dust cake

μ = viscosity of fluid

ρ_p = density of dust particle

ε = porosity of dust cake.

The permeability, k, may be determined using various models for dilute assemblages of particles [21-25]; the structure of the dust cake around individual fibers is then eliminated completely. Such an approach is valid only in the later stages of filtration when the filter is clogged and the dust forms a continuous cake on the surface (typically $M > 50$ mg/cm^2) [20].

When an electric field is applied, however, the dust has a greater tendency to deposit around fibers, clogging is impeded, and the presence of the fibers remains important for larger loadings. A specific cake resistance model is inappropriate, particularly for determining the influence of the microcake structure on the overall drag.

The approach taken here is to assume the fiber matrix remains important, which is true even for the no-field case at low loadings. The clean filter model is now written in terms of porosity, rather than fiber volume fraction, to include the space occupied by the dust and an effective radius that reflects the microstructure of the dust cake:

$$\frac{\Delta p R^2}{\mu U h} = f(\varepsilon) \ , \qquad (4)$$

where

$$f(\varepsilon) = \frac{4\,(1-\varepsilon)}{-\ln(1-\varepsilon) + 2(1-\varepsilon) - \frac{(1-\varepsilon)^2}{2} - \frac{3}{2}}$$

ε = porosity = $1 - c - \beta$
β = volume fraction of dust, $M/\rho_p h$
R = effective dust cake-fiber radius

The dust cake structure is modeled in three ways: (1) a uniform deposition model which assumes all the dust deposits uniformly around individual fibers so that R increases uniformly with β, (2) a dendrite model which assumes that all the dust deposits as particle-particle chains, and (3) a combined model which is a combination of the first two through an adjustable parameter called the dendrite fraction (DFR).

The presence of dendrites has been noted in the literature, particularly during the early stages of deposition. Wang et al. [25] used a stochastic simulation model to show how dendrites form when no field is present. Oak and Saville [26] showed how dendrites build up on a single fiber placed in an electric field. Payatakes [27,28] developed a model for the growth of dendrites and their effect on drag, which unfortunately has too many parameters to be of practical use. Pense et al. [29] obtained estimates for the drag on ideal dendrite structures on a model collector.

Bergman et al. [17] simply modeled the dendrites as another set of fibers in the filter but with a diameter corresponding to the particle diameter. They found that the dust represented as dendrites gives a greater pressure drop than uniform deposition around fibers and suggested that the number of dendrites is smaller when an electric field is present. A similar approach is taken here.

Case 1: Uniform Deposition

In this case the dust particles are assumed to deposit uniformly around each fiber as shown in Figure 47a. If the volume fractions of fiber and dust are c and β_1, respectively, the effective radius of the fiber-dust aggregate, R, is given by

$$\pi R^2 \ell = C + \beta_1 = 1 - \varepsilon \quad , \tag{5}$$

where $\ell = c/\pi a^2$ = length of fiber per unit volume of filter

$$\beta_1 = \frac{\beta}{1-\varepsilon_c} = \frac{M}{h\rho_p(1-\varepsilon_c)} = \text{volume of dust}$$

ε_c = porosity of dust cake around fibers
M = mass of dust accumulated per area of filter
h = depth of filter
ρ_p = density of dust particle

Therefore,

$$R^2 = \left(\frac{1-\varepsilon}{c}\right)a^2 \quad . \tag{6}$$

Special care has been taken to define the volume occupied by the dust, β_1, which must include the porosity of the dust cake around the fibers, ε_c. It is shown in Appendix 9A at the end of this section that, for typical dust cake permeabilities, the drag on a porous cylinder is the same as the drag on a solid cylinder of the same dimensions. Thus, the voids in the dust cake are not included in the overall porosity as defined by Equation 5, and so the value of ε_c directly affects the overall porosity as well as the effective fiber radius.

Substituting Equation 6 into Equation 4, the expression for uniform deposition is obtained:

$$\frac{\Delta p a^2}{\mu U h} = \frac{c}{1-\varepsilon} f(\varepsilon) \quad . \tag{7}$$

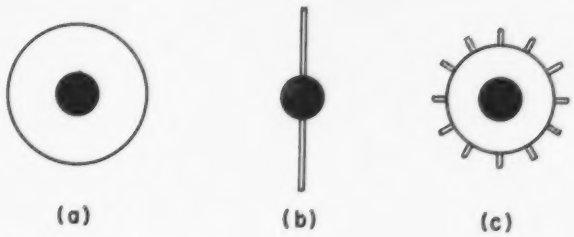

Figure 47. Dust cake representations.
a) Uniform depostion model b) Dendrite model c) Combined model

Case 2: Dendrite Model

Here the filter is modeled as having two sets of fibers, one of radius a and the other with radius r_d, the mean radius of the dendrites. The radius of the dendrites can be related to the mean radius of the particles, r_p, by assuming the particles are spherical. Thus, r_d is given by the radius of the cylinder of length $2r_p$ and equal in volume to the spherical particle:

$$\pi r_d^2 (2r_p) = \frac{4}{3}\pi r_p^3 \quad ,$$

$$r_d^2 = \frac{2}{3} r_p^2 \quad . \tag{8}$$

The volume surface average radius,

$$R = \frac{\Sigma \ell_i r_i^2}{\Sigma \ell_i r_i} \quad ,$$

where ℓ_i = length of fibers of radius r_i per unit volume of filter,

proposed by Chen [30] and by Wheat [31], can be used to find the effective radius of fibers in a filter of more than one fiber diameter. Data from packed column experiments confirm this as does hydraulic radius theory [24]. Thus

$$R = \frac{\ell_d r_d^2 + \ell a^2}{\ell_d r_d + \ell a} \quad . \tag{9}$$

Since $\ell_d = \frac{\beta}{\pi r_d^2}$,

$$\ell = \frac{c}{\pi a^2} \quad ,$$

and $\varepsilon = 1-(\beta+c)$,

Equation 9 becomes $R = \frac{(1-\varepsilon) r_d a}{\beta a + c r_d}$.

Substituting into Equation 4, the final form of the dendrite model is

$$\frac{\Delta p a^2}{\mu U h} = \frac{1}{(1-\varepsilon)^2} \frac{(\beta a + c r_d)^2}{r_d^2} f(\varepsilon) \quad . \tag{10}$$

Case 3: Combined Model

The uniform deposition model and the dendrite model are combined with the adjustable parameter DFR, the fraction of dust depositing as dendrites. Let

$$\varepsilon = 1 - c - \beta_1 - \beta_2 \quad , \tag{11}$$

where β_1 = volume of the uniform dust cake around individual fibers per unit volume

$$= (1-DFR)\beta/(1-\varepsilon_c)$$

β_2 = volume fraction of dust deposited as dendrites

$$= DFR \cdot \beta$$

From Equations 6 and 9, the radius of the uniform part of the dust deposit around the fiber, r_u, and the effective radius of the fiber-dust aggregate, R, are given by

$$r_u^2 = \left(\frac{c+\beta_1}{c}\right) a^2$$

and

$$R = \frac{\ell_d r_d^2 + \ell r_u^2}{\ell_d r_d + \ell r_u} \quad .$$

Here again,

$$\ell_d = \frac{\beta_2}{\pi r_d^2} \quad \text{and} \quad \ell = \frac{c}{\pi a^2} \quad ,$$

so that

$$R = \frac{(1-\varepsilon) r_d a}{\beta_2 a + [c(c+\beta_1)]^{\frac{1}{2}} r_d} \quad .$$

Substituting into Equation 4,

$$\frac{\Delta p a^2}{\mu U h} = \frac{1}{(1-\varepsilon)^2} \frac{\{\beta_2 a + [c(c+\beta_1)]^{\frac{1}{2}} r_d\}^2}{r_d^2} f(\varepsilon) \tag{12}$$

Notice that the pressure drop is a nonlinear function of the parameter DFR.

Fiber Volume Fraction Distribution

In general, both c and β are functions of z, the depthwise distance into the filter. At the upstream surface, z = 0; z = 1 at the downstream surface. Suppose that the filter consists of n layers of thickness Δz_i h, where i = 1 to n, and that the sum of the pressure drops across each layer is equal to the total pressure drop:

$$\frac{\Delta p a^2}{\mu U h} = \sum_{i=1}^{n} \frac{1}{r_d^2} \frac{\{\beta_2(z_i)a + [c(z_i)(c(z_i)+\beta_1(z_i)]^{\frac{1}{2}} r_d\}^2}{(1-\varepsilon(z_i)^2} \Delta z_i \quad (13)$$

The combined model (Equation 12) has been used for the pressure drop across each layer. If we take the limit as $n \to \infty$ and $\Delta z_i \to 0$, we obtain the integral form of this equation:

$$\frac{\Delta p a^2}{\mu U h} = \frac{1}{r_d^2} \int_0^1 \frac{\{\beta_2(z)a + [c(z)(c(z)+\beta_1(z))]^{\frac{1}{2}} r_d\}^2}{(1-\varepsilon(z))^2} dz \quad (14)$$

The validity of Equations 13 and 14 depends on the assumption that the pressure drops across the individual layers are additive. To test this assumption, a series of experiments were performed on the column apparatus with the column packed so that there were regions of differing c. The pressure drop was measured across each region, and to within experimental error, the sum of the pressure drops across each region did equal the total pressure drop across the column. Entrance and exit effects were also minimal. Thus, the assumption seems to be in good order.

RESULTS AND DISCUSSION

Implications of the Combined Model

The parameters in the model fall into three categories: properties of the aerosol, properties of the filter, and properties of the dust cake structure. The properties of the aerosol include U, μ, r_p, and ρ_p. A typical value for the face velocity for baghouse filtration is 1 cm/s; ESFF may allow face velocities of 3 cm/s or more. The viscosity of air, μ, is taken to be 0.018 cp. The size distribution of a sample of fly ash used in the experiments in the preceding section is given in Appendix A of Section 8, and the mean radius was found to be $\sim$3.0 μm. The density of the fly ash particles was 2.2 gm/cm^3.

The properties of the filter needed in the model are a, h, and c. These parameters depend on the fiber material and the filter construction (nonwoven, needlepunched, woven, etc.) and so must be measured for the filter under consideration. Typical values for a are 5-15 μm, and c is usually less than 0.25 but may vary with depth.

The dust cake parameters are M, ε_c, and DFR. Since the model was developed for light loadings, M should be kept below 50 mg/cm^2. Billings

and Wilder [20] state that no porosity measurements have been made for cakes on operating filters, but they probably range from 0.4 to 0.9 depending on the particle size and on the pressure drop, the face velocity, adhesion effects, humidity, and electrostatic forces. They present data for the bulking properties of various powders. For a surface mean diameter of 3 μm (the mean diameter of the fly ash sample in Appendix 8A, Section 8), ε ranges from 0.6 to 0.7. Other data for silicates, also compiled in Billings and Wilder, give ε = 0.64. Dennis and Dirgo [32] assumed a value of 0.59 for fly ash in their K_2 calculation.

Rudnick and First [21] state that most values for cake porosity found in the literature have apparently been obtained by placing the dust in glass containers and tapping, which can lead to considerable error. They measured cake porosities in situ for dust cakes of AC-fine test dust with a surface mean diameter of ∿1.2 μm and obtained values ranging from 0.85 to 0.92. The dendrite fraction parameter, DFR, can be qualitatively determined from observation of filter deposits. Quantitative determination of DFR will have to come from fitting the data with the model.

To test the sensitivity of the model to the dust cake parameters, values of 10 μm and 0.5 mm were assigned to the filter parameters a and h, respectively. Two values of c were used, 0.02 and 0.2, to simulate low and high density regions in an industrial filter.

Figure 48 shows how the predicted pressure drop varies with the dust loading, M, for the two values of c. The values of DFR and ε_c are fixed at 0.25 and 0.7, respectively. As expected, the pressure drop at a given dust loading is less for c = 0.02 than for c = 0.2, indicating that lower density regions have a greater capacity for dust accumulation. The concave upward form of the curve is consistent with experimental observations (Figure 43). The slow rising section at low M is attributed to the clogging of the pores within the fabric. This is followed, in a real filter, by a linear region which represents the steady buildup of a uniform dust cake. The model, however, has no provision for a buildup of a continuous dust cake, and thus, as the filter approaches a clogged state, the pressure drop increases without bound. A more detailed discussion of this limitation of the model is presented below.

Figure 49 shows how the pressure drop varies with ε_c. The dust loading is a constant 5 mg/cm^2 and the dendrite fraction is 0.25. The pressure drop changes little until ε_c reaches 0.7, above which, especially between 0.8 and 0.9, the pressure drop is very sensitive to the value of ε_c. Pressure drop is also more sensitive to ε_c for larger values of c.

In Figure 50, pressure drop is presented as a function of DFR. Here, M = 5 mg/cm^2 and ε_c = 0.60. The pressure drop increases with increasing DFR, and is more sensitive to DFR at lower values of c; in this example, increasing DFR from 0 to 1 increased the pressure drop by a factor of 30 for c = 0.02 but only by a factor of 3 for c = 0.2.

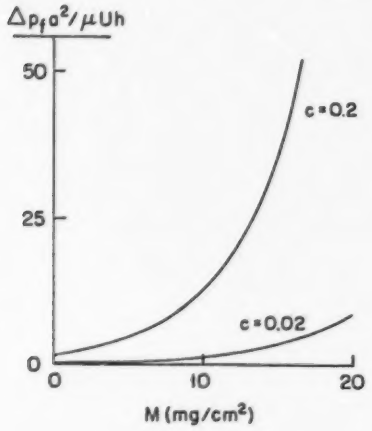

Figure 48. Model results: pressure drop vs. dust loading. ε_c = 0.7, DFR = 0.25, h = 0.5 mm, a = 10 μm, r_p = 3 μm.

Figure 49. Model results: pressure drop vs. ε_c at constant M = 5 mg/cm². DFR, h, a, r_p as in Figure 48.

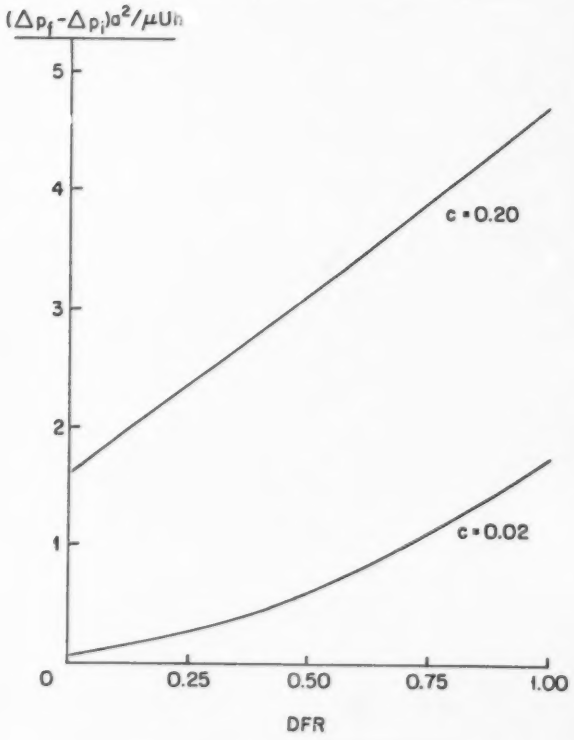

Figure 50. Model results: pressure drop vs. DFR at constant M = 5 mg/cm². ε_c, h, a, and r_p as in Figure 48.

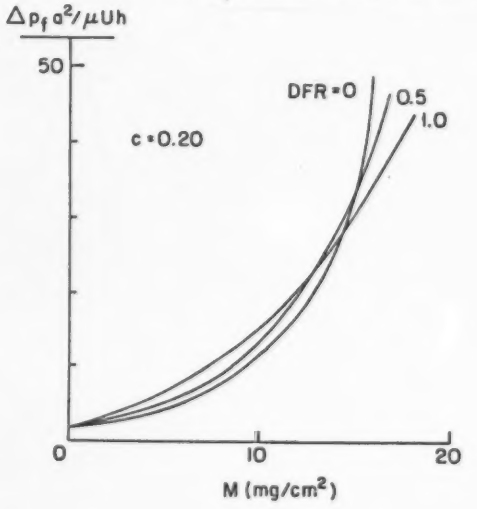

Figure 51. Model results: pressure drop as a function of M and DFR. ε_c, h, a, and rp as in Figure 48.

The crossing of the curves at high values of M depicted in Figure 51 occurs in the regime where the validity of the model is questionable. As mentioned above, the model continues to place dust inside the filter after it is clogged rather than forming a constant porosity dust cake on top. The model packs the dust in the filter tighter than it would naturally deposit, decreasing the overall porosity to a point where the mathematical equation becomes singular. This results in the anomalous behavior at high M found in Figure 51.

Equation 4 may be rewritten as

$$\frac{\Delta p a^2}{\mu U h} = (a^2 R^{-2})\, f(\varepsilon) \quad , \tag{15}$$

where both R and ε are functions of the dust loading. Figure 52 shows how the competing effects of a^2/R^2 and $f(\varepsilon)$, when multiplied together, result in the pressure drop across the filter as a function of M. The example considered here is for DFR = 0, $\varepsilon_c = 0.7$, and c = 0.20. The quantity a^2/R^2 decreases slowly, only by a factor of 4 over the range of $(1-\varepsilon)$ considered, whereas $f(\varepsilon)$ increases substantially, by almost three orders of magnitude. Clearly the effect of dust loading on $f(\varepsilon)$ dominates at the higher value of M; the pressure drop closely tracks $f(\varepsilon)$, which rapidly rises as $\varepsilon \to 0$.

At lower values of c, the relationship between M and ε (Equation 5) is changed by the value of c, so that more dust can be loaded in the filter to produce the same value of ε. Thus $f(\varepsilon)$ does not rise as fast with increasing M. Furthermore, as shown by Equation 6, a^2/R^2 decreases more rapidly with increasing M. Therefore, the pressure drop rises more slowly with increasing dust loading at smaller values of c.

The effect of DFR on the pressure drop calculation can also be explained by looking at these competing effects. The presence of dendrites shows the growth of R since cylinders of a smaller radius must be averaged in with the fiber-dust cake structures. This has the effect of increasing a^2/R^2 and increasing the pressure drop.

The dendrites also increase ε from what it would be in the uniform deposition model, since the dendrites do not have a void volume associated with them that is excluded in the computation of ε. (Recall that the dust cake around the fibers, with porosity ε_c, is assumed to be impermeable and its void volume is excluded from ε.) This has the effect of decreasing $f(\varepsilon)$ and hence pressure drop.

For small values of M, the effect of the dendrites on the R^2 term dominates, and the pressure drop increases with larger values of DFR. At larger values of M (smaller values of ε), $f(\varepsilon)$ rises rapidly and the effect on ε dominates, leading to the crossover observed in Figure 51. However, at these low values of ε the model is no longer valid; clogging almost certainly has occurred and such values of ε are physically unrealistic.

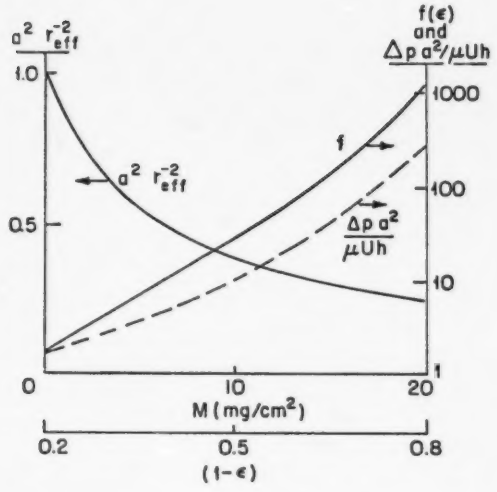

Figure 52. The effect of dust loading on a^2R^{-2} and $f(\varepsilon)$ and the resulting pressure drop. $\varepsilon_c = 0.7$, a = 10 μm, h = 0.5 mm, DFR = 0.

Finally, the effect ε_c has on the pressure drop, in light of this analysis, is simply to change the relationship between M and ε (see Equation 5). Thus, in Figure 52, the bottom scale will change with ε_c. Increasing ε_c decreases the value of ε for a given M, and hence the curves are shifted to the left, and vice versa.

In the preceding analysis it has been shown that the model is inappropriate for high values of M. The most important parameter determining the limiting value of M is the overall porosity, ε. It appears that for $\varepsilon < 0.35$, $f(\varepsilon)$ rises too rapidly for the model to predict reasonable values. This porosity approaches that of the closest packed arrangement for spheres, and thus porosities below this are probably unrealistic and indicate the filter is clogged. The limiting value of M thus depends on this limiting value of ε through Equation 11 and the parameters c, h, DFR, and ε_c.

Comparison with Experimental Data

The model results are now compared with experimental data presented in the preceding section describing two-layer filter experiments. The dust in the low density upstream layer was found to be partitioned into two regions; more dust deposited near the surface of the layer either because of the increase in capture efficiency of the upstream fibers induced by the electric field, or, when no field was present, because of clogging phenomena. The surface buildup of dust with no field was found to be a function of dust loading in the low density layer. From the data in the preceding section this relationship is estimated to be

$$M_s = 0.86\ M_1 - 0.62 \quad , \tag{16}$$

where M_s = surface buildup of dust (mg/cm^2), M_1 = total dust loading in layer (mg/cm^2).

These filters can conveniently be modeled as four layers, as shown in Figure 53. The top two layers (c = 0.017) represent the fluffy upstream layer and the low density surface regions of the downstream layer.

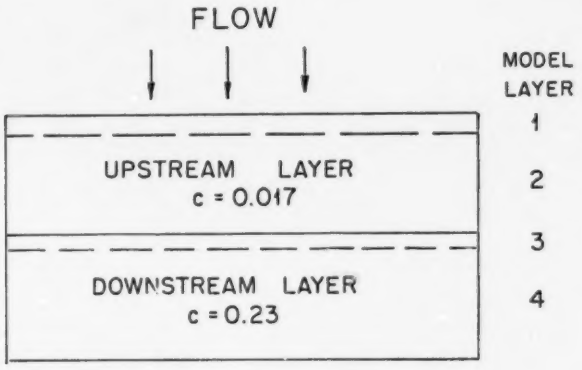

Figure 53. Schematic of model representation of experimental two-layer filters.

Layer 1 corresponds to the region where the surface buildup of dust occurs. The bottom two layers (c = 0.23) represent the high density downstream layer in the experimental filters with layer 3 being the thin region where any dust that penetrates the low density region collects. Layers 1 and 2 are collectively referred to as the upstream layer and any dust that is said to collect in the upstream layer is apportioned to layers 1 and 2 according to Equation 16. Similarly, layers 3 and 4 are called the downstream layer. Any dust collecting in the downstream layer is put in layer 3; it is assumed that no dust deposits in layer 4.

Table 12 lists the physical parameters for each of the 4 layers. The depths of layers 1 and 3 were estimated from cross-sectional views of the dust laden filters. All the other parameters correspond to measured values of the experimental filters except the radii of the fibers in layers 3 and 4. It was found that the Happel model overestimates the pressure drop at high values of c (this can be seen to some extent in Figure 46); the value of a was increased from 10 to 12 μm to correct for this. The value of r_p was taken to be 3 μm and of U to be 3 cm/s.

TABLE 12. PHYSICAL PROPERTIES OF MODEL FILTER

Layer	c	h (mm)	a (μm)
1	0.017	0.3	9
2	0.017	1.3	9
3	0.23	0.2	12
4	0.23	1.5	12

Figure 54 compares model predictions with data taken by loading each layer with dust separately, without the other being present, and measuring the pressure drop. No electric field was applied. The curves calculated for DFR = 0.25 show that a value of 0.7 for the parameter ε_c best fits the data. Using a DRF of 0.5 gives slightly better results, but such a high percentage of dendrites is not supported by visual observations of the cake structure.

Even with the fitted parameters, the general shapes of the curves in Figure 54 are not in total agreement with the data. The curves increase too slowly with M for small M, and too rapidly for larger M. The point where they begin to overpredict the pressure drop is in the regime where ε is too small and the model is no longer valid (in the upstream layer $\varepsilon = 0.36$ at M = 15 mg/cm^2, and in the downstream layer $\varepsilon = 0.33$ at M = 7 mg/cm^2).

Nevertheless, the fit is good enough to compare the model with some other results. In Figure 55 the results of a series of experiments on the two-layer filters taken at a constant dust loading of 11.9 mg/cm^2 are presented. The electric field strength was varied, shifting the proportion of dust between the two layers; increasing the field strength increased the amount of dust in the upstream layer. As shown in Figure 55, the model, using the fitted parameters $\varepsilon = 0.7$ and DFR = 0.25, correctly predicts the reduction in pressure drop as a greater fraction of dust is deposited in the upstream layer. A DFR of 0.50 works better at low dust fractions in the upstream layer, since the corresponding high dust loadings in the high density downstream layer press the limit of validity of the model.

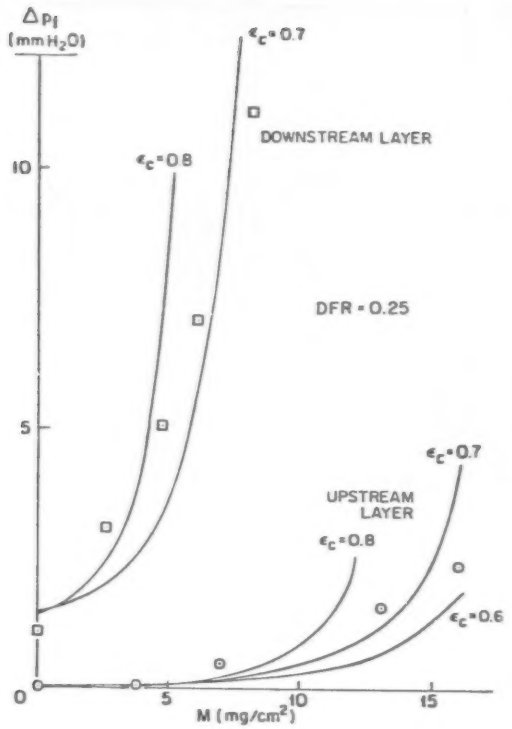

Figure 54.

Comparison of model results with single-layer experimental results at 0 kV applied potential.

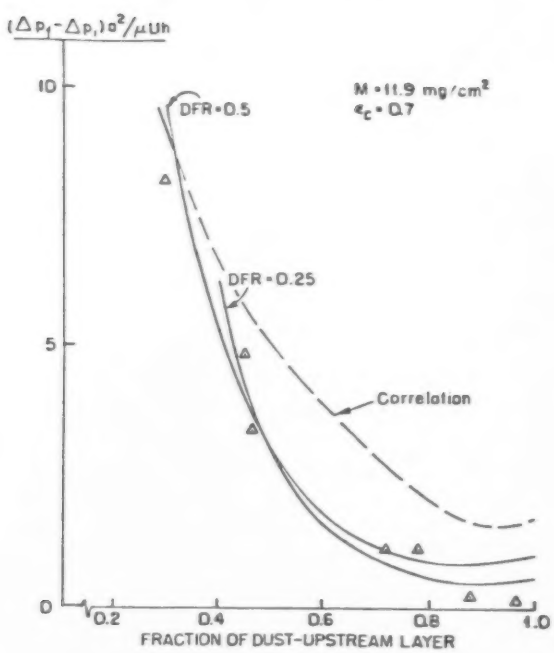

Figure 55

Comparison of model predictions with two-layer experiments at a constant dust loading. The dust distribution was shifted upstream by increasing the applied electric field strength. The dashed curve represents a correlation of the data in Figure 54.

The agreement between model prediction and experiment is remarkable but may be due, in part, to the underprediction of the model at low dust loadings. Indeed, correlating the data of Figure 54 and comparing it with the data of Figure 55 (dashed line) shows less agreement, although the general trend is the same. Both the model and correlation overpredict the data at high dust fractions in the upstream layer. This is due to lateral displacements of the dust on the surface at high electric field strengths, which is not taken into account by the model or correlation of 0 kV data.

In conclusion, we see that the mathematical model that has been developed predicts the pressure drop across a fabric filter during the initial stages of filtration before clogging of the filter has been completed and a continuous dust cake forms. The model incorporates information on the microstructure of the dust cake as well as the fiber volume fraction distribution in the filter. Specific conclusions concerning the results of the model predictions are summed up as follows:

1. The model is limited to $\varepsilon > 0.35$ as computed by Equation 11. Below this limit the model becomes singular.

2. The model is sensitive to the parameters ε_c and DFR, indicating that the microstructure of the dust cake plays an important role in determining the pressure drop.

3. The model shows that just shifting the dust distribution upstream to regions of lower fiber volume fraction substantially reduces the pressure drop, which indicates that this mechanism plays a significant role in ESFF.

APPENDIX 9A. DRAG ON AN ISOLATED POROUS CYLINDRICAL ANNULUS IN CREEPING FLOW

In order to gain insight into how dust aggregates surrounding fibers affect drag, the problem of drag on an isolated porous annulus in creeping flow was solved.

Consider two concentric, infinite cylinders of radii R_1 and R_2 situated normal to a uniform flow field as in Figure 9A1. Let region I outside both

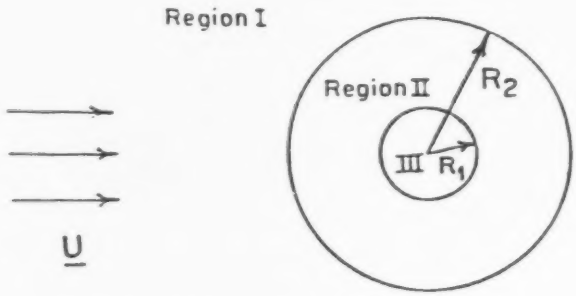

Figure 9A1. The porous cylinder problem.

cylinders be completely permeable and the annular region II between the two cylindrical surfaces have a permeability k. Region III, the innermost region, is impermeable. The governing equations for fluid flow in each region are

Region I $(r > R_2)$

$$-\nabla p_1 + \mu \nabla^2 \underline{u}_1 = 0 \tag{A1}$$

$$\nabla \cdot \underline{u}_1 = 0 \tag{A2}$$

Region II $(R_1 < r < R_2)$

$$-\nabla p_2 + \mu' \nabla^2 \underline{u}_2 = \frac{\mu'}{k} \underline{u}_2 \tag{A3}$$

$$\nabla \cdot \underline{u}_2 = 0 \tag{A4}$$

The boundary conditions are

$$\text{at } r = R_1 \qquad \underline{u}_2 = 0 \tag{A5}$$

$$\text{at } r = R_2 \qquad \underline{u}_1 = \underline{u}_2 \tag{A6}$$

$$\sigma_1 \cdot \underline{n} = \sigma_2 \cdot \underline{n} \tag{A7}$$

$$\text{as } r \to \infty \qquad \underline{u}_1 \to \underline{U} \tag{A8}$$

Here $\underline{u}_1$ and p_1 are the average velocity and pressure drop in region I; $\underline{u}_2$ and p_2 are their counterparts in region II. $\underline{U}$ is the uniform, free stream velocity, μ' is the effective viscosity of the fluid in region II, and μ is the fluid viscosity.

In region I, the equations of motion for slow viscous flow reduce to the Stokes equation (A1). However, as Stokes' paradox informs us, the solution to the Stokes equation for unbounded planar flow past an infinite cylinder is nonexistent; boundary condition (A8) cannot be satisfied. Scaling arguments show that, while the Stokes equation is valid close to the surface of the cylinder, far away from the cylinder the Oseen approximation to the Navier-Stokes equation is more appropriate:

$$\rho \underline{U} \cdot \nabla \underline{u}_1 = -\nabla p_1 + \mu \nabla^2 \underline{u}_1 . \tag{A9}$$

The full solution to the flow field in region I can be obtained by matching the "inner" Stokes solution with the "outer" Oseen solution using the method of matched asymptotic expansions [33].

Rather than Darcy's law, Brinkman's equation [22] has been used in region II since it can account for the boundary layer at the porous media-free stream interface [34]. This is preferable to using Darcy's law and imposing a slip velocity condition at the interface [35,36]. For simplicity, it was assumed that the effective viscosity of the fluid in the porous medium, μ', was equal to the fluid viscosity, μ. This is consistent with the analysis of several others [22,34,37,38].

The boundary conditions are straightforward. (A5) is the no slip condition at the solid cylinder surface. (A6) and (A7) are the conditions of continuity of velocity and stress (normal and shear) at the porous media-free stream interface. (A8) is the requirement that far away from the cylinder the velocity equals the free stream velocity.

The solutions to the fluid flow equations in each region, given in terms of the stream function, ψ, defined by

$$v_r = \frac{1}{r} \frac{\partial \psi}{\partial \theta}$$

and

$$v_\theta = - \frac{\partial \psi}{\partial r}$$

where $\underline{v} = \underline{u}_1$ in region I,

and $\underline{u}_2$ in region II,

are

$$\psi_I = U \sin\theta \left(\ln \frac{Re}{8} + C_1 - 1 + \gamma\right)^{-1} \left(-r \ln r + C_1 r + C_2 r^{-1}\right) \qquad \text{(A10)}$$

and

$$\psi_{II} = U \sin\theta \left\{\frac{C_3}{\Phi^2 r} + \frac{C_4 r}{\Phi^2} + C_5 K_1 (\Phi r) + C_6 I_1 (\Phi r)\right\} . \qquad \text{(A11)}$$

Here, $\Phi = R_2/\sqrt{k}$

K_1, I_1 = modified Bessel functions of order one

γ = Euler's constant = 0.5772...

Re = Reynolds number = $2\rho U R_2/\mu$

$C_1 \ldots C_6$ = constants

The drag per unit length acting on the cylinder, F_D, is found to be

$$F_D = \frac{-4\pi\mu U}{\ln \frac{Re}{8} + C_1 - 1 + \gamma} \qquad \text{(A12)}$$

where C_1 is the coefficient of the r term in equation (A10). If region II is impermeable, $C_1 = 0.5$.

The coefficients in equations (A10) and (A11), $C_1, \ldots, C_6$, can be obtained by applying the boundary conditions (A5) through (A7). (Condition (A8) has already been used to find ψ_I.) The six boundary conditions generate six algebraic equations for the six unknown coefficients which were solved numerically for various values of Re and R (= R_1/R_2). The results for Re = 0.2 are shown in Figure 9A2. Here, the dimensionless drag, $F_D/\mu U$, is plotted against the parameter Φ (= $R_2/\sqrt{k}$).

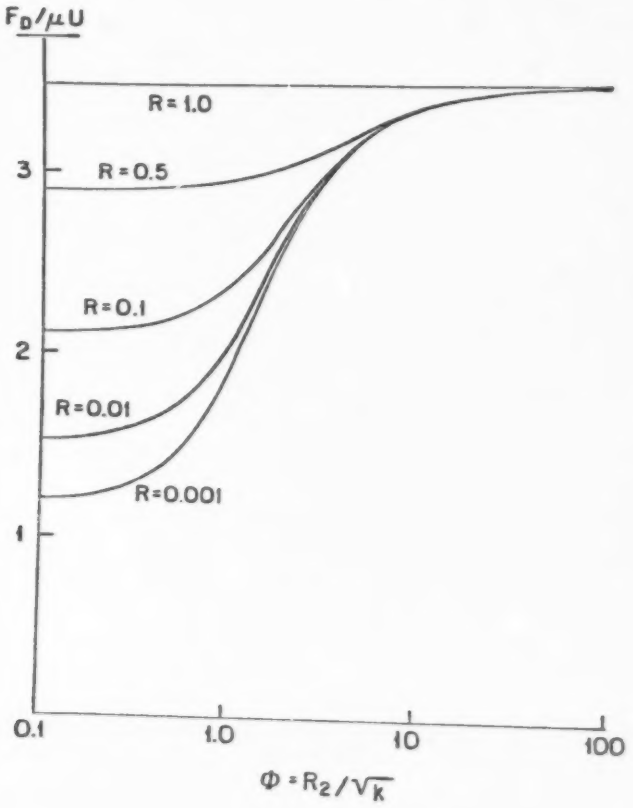

Figure 9A2. Drag on a porous cylinder for a Reynolds number ($2\rho UR_2/\mu$) of 0.2 as a function of permeability k and radius ratio $R = R_1/R_2$.

The results point out the obvious: at low Φ (high permeability), the drag asymptotically approaches the drag on an isolated cylinder of radius R_1; region II becomes so porous that it does not exert any drag at all. At high Φ (low permeability), the drag approaches the drag on an isolated cylinder of radius R_2; region II becomes solid-like. The interesting aspect of the results, however, is the range of values of k for which the porous region is, for practical purposes, solid-like. In Table 9A1, values of Φ are presented which were calculated by using Rudnick and First's [21] model for the permeability of a dilute assemblage of fly ash particles with the size range distribution given in Appendix 8A, Section 8. Even at high porosities, Φ is greater than 10, indicating that the dimensionless drag is greater than 3.35 or 97% of the drag on a solid cylinder of radius R_2. This leads to the conclusion that dust cake structures around individual fibers, even if they contain only 10% solids, behave like solid structures of the same overall dimensions.

TABLE 9A1. PERMEABILITY PARAMETER Φ FOR SEVERAL POROSITIES, ε, AS COMPUTED FROM RUDNICK AND FIRST'S MODEL [21]

ε	$K_2(s^{-1})$	$k(cm^2)$	Φ	
			R_2 = 30 μm	R_2 = 100 μm
0.6	1.63×10^{5}	1.25×10^{-9}	57	283
0.7	1.00×10^{5}	2.73×10^{-9}	38	190
0.8	6.3×10^{4}	1.00×10^{-8}	20	100
0.9	4.0×10^{4}	2.00×10^{-8}	14	70

REFERENCES

1. Miller, B., Lamb, G.E.R., Costanza, P., Saville, D.A., and Oak, M.J. Studies of Dust Cake Formation and Structure in Fabric Filtration. EPA-600/9-81-023. U.S. Environmental Protection Agency, Research Triangle Park, N.C., 1983.

2. Lamb, G.E.R., Costanza, P.A., and O'Meara, D.J. Electrical Stimulation of Fabric Filtration. Part II: Mechanism of Particle Capture and Trials with a Laboratory Baghouse. Textile Res. J. 48: 566-573, 1978.

3. Lamb, G.E.R., and Costanza, P.A. Electrical Stimulation of Fabric Filtration Part III: Effects of Electrode Current. Textile Res. J. 51: 389-398, 1981.

4. Van Osdell, D., Greiner, G.P., Lamb, G.E.R., and Hovis, L.S. Electrostatic Augmentation of Fabric Filtration. In: Proceedings of the Third Symposium on the Transfer and Utilization of Particulate Control Technology, Orlando, Flordia, 1981. Vol. 1, pp. 35-44.

5. Chiang, T., Samuel, F.A., and Wolpert, K.E. Theoretical Aspects of Pressure Drop Reduction in a Fabric Filter with Charged Particles. In: Proceedings of the Third Symposium on the Transfer and Utilization of Particulate Control Technology, Orlando, Florida, 1981. Vol. III, pp. 250-260.

6. Donovan, R.P., Hovis, L.S., and Abbott, J.H. Pulse-jet Filtration with Electrically Charged Fly Ash. In: Proceedings of the Third Symposium on the Transfer and Utilization of Particulate Control Technology, Orlando, Florida, 1981. Vol. I, pp. 11-22.

7. Cooper, D.W., and Rei, M.T. Evaluation of Electrostatic Augmentation for Fine Particle Control. EPA-600/2-76-055. March 1976.

8. Page, L., and Adams, N.I., Jr. Principles of Electricity. D. Van Nostrand Co. Inc., New York, 1949. p. 102.

9. Van Osdell, D.W., Ranade, M.B., Greiner, G.P., and Furlong, D.F. Electrostatic Augmentation of Fabric Filtration: Pulse-jet Pilot Unit Experience. EPA-600/7-82-062 (NTIS PB83-168625), November 1982.

10. Penney, G.W. Electrostatic Effects on Fabric Filtration,Vol. I. EPA-600/7-78-142a (NTIS PB 288576), September 1978.

11. Lamb, G.E.R. and Costanza, P.A. Role of Filter Structure and Electrostatis in Dust-Cake Formation. Textile Res. J. 50: 661-667, 1980.

12. Lamb, G.E.R., and Costanza, P.A. Influences of Fiber Geometry on the Performance of Nonwoven Air Filters, Part III: Cross-Sectional Shape. Textile Res. J. 50: 362-370, 1980.

13. Leith, D., First, M.W., and Gibson, D.D. Effect of Modified Cleaning Pulses on Pulse Jet Filter Performance. Filtration and Separation 15: 400, 1978.

14. Dennis, R., and Wilder, J. Fabric Filter Cleaning Studies. EPA-650-2-75-009.

15. Lamb, G.E.R., Costanza, P.A., and Turner, J.H. Role of Filter Structure and Electrostatics in Dust-Cake Formation. Textile Res. J.: 50, 661-667, 1980.

16. Oak, M.J. Fibrous Filtration in Presence of Electric Fields. Ph.D. Dissertation. Department of Chemical Engineering, Princeton University, 1981.

17. Bergman, W., Taylor, R.D., Miller, H.H., Biermanns, A.H., Hebard, H.D., da Roza, R.A., and Lum, R.Y. Enhanced Filtration Programs at Lawrence Livermore Laboratory - A Progress Report. 15th D.O.E. Air Cleaning Conference, Boston, Mass., August 1978.

18. Felix, L.G., and Smith, W.B. Preservation of Fabric Filtered Dust Cake Samples. J. Air Pollution Control Assoc.: 33, 1092, 1983.

19. Happel, J. Viscous Flow Relative to Arrays of Cylinders. AIChE J.: 5, 174, 1959.

20. Billings, C.E., and Wilder, J. Handbook of Fabric Filter Technology, Vol. I, Fabric Filter Systems Study, GCA/Technology Division. EPA No. APTD 0690 (NTIS No. PB-200-648), December 1970.

21. Rudnick, S.N., and First, M.W. Specific Resistance (K_2) of Filter Dust Cakes: Comparison of Theory and Experiments. In: Third Symposium on Fabric Filters for Particulate Collection. EPA-600/7-78-087, June 1978.

22. Brinkman, H.C. A Calculation of the Viscous Force Exerted by a Flowing Fluid on a Dense Swarm of Particles. Appl. Sci. Res.: A1, 27, 1947.

23. Hinch, E.J. An Averaged-Equation Approach to Particle Interactions in a Fluid Suspension. J. Fluid Mech.: 83, 695, 1977.

24. Scheideggar, A. E. The Physics of Flow through Porous Media, University of Toronto Press, Great Britain, 1963.

25. Wang, C., Beizaie, M., and Tien, C. Deposition of Solid Particles on a Collector: Formulation of a New Theory. AIChE J.: 23, 879, 1977.

26. Oak, M. J., and Saville, D. A. The Buildup of Dendrite Structures on Fibers in the Presence of Strong Electrostatic Fields. J. Coll. Interface Sci.: 76, 259-62, 1980.

27. Payatakes, A. C. Model of Dynamic Behavior of a Fibrous Filter. Application to Case of Pure Interception During Period of Unhindered Growth. Powder Tech.: 14, 267, 1976.

28. Payatakes, A. C. Model of Transient Aerosol Particle Deposition in Fibrous Media with Dendrites Pattern. AIChE J.: 23, 192, 1977.

29. Pense, H., Tien, C., and Turian, R. M. Drag Force Measurements of Single Spherical Collectors with Deposited Particles. AIChE J.: 27, 364, 1981.

30. Chen, C. Y. Filtration of Aerosols by Fibrous Media. Chem. Revs.: 55, 595, 1955.

31. Wheat, J. A. The Air Flow Resistance of Glass Fiber Filter Paper. Can. J. Chem. Engr.: 41, 67, 1963.

32. Dennis, R., and Dirgo, J. A. Comparison of Laboratory and Field Derived K_2 Values for Dust Collected on Fabric Filters. Filtration and Separation: 18, 394, 1981.

33. Van Dyke, M. Perturbation Methods in Fluid Mechanics. The Parabolic Press, Stanford, California, 1975.

34. Neale, G., Epstein, N., and Nader, W. Creeping Flow Relative to Permeable Spheres. Chem. Engr. Sci.: 28, 1865-1874, 1973.

35. Beavers, G. S. , and Joseph, D. D. Boundary Conditions at a Naturally Permeable Wall. J. Fluid Mech.: 30, 197, 1967.

36. Saffman, P. G. On the Boundary Condition at the Surface of a Porous Medium. Studies in Appl. Math.: 50, 93-101, 1971.

37. Howells, I. D. Drag Due to the Motion of a Newtonian Fluid Through a Sparse Random Array of Small Fixed Rigid Objects. J. Fluid. Mech.: 64, 449-475, 1974.

38. Higdon, J.J.L., and Kojima, M. On the Calculation of Stokes' Flow Past Porous Particles. Int. J. Multiphase Flow: 7, 719-727, 1981.